

Thermoelastic properties of synthetic single crystal portlandite $\text{Ca}(\text{OH})_2$ - Temperature-dependent thermal diffusivity with derived thermal conductivity and elastic constants at ambient conditions

S. Breuer^{a,*}, M. Schwotzer^b, S. Speziale^c, F.R. Schilling^a

^a Karlsruhe Institute of Technology (KIT), Institute of Applied Geosciences (AGW), Adenauerring 20b, 76131 Karlsruhe, Germany

^b Karlsruhe Institute of Technology (KIT), Institute of Functional Interfaces (IFG), Hermann-von-Helmholtz-Platz 1, 76344 Eggenstein-Leopoldshafen, Germany

^c German Research Centre for Geosciences (GFZ), Helmholtz Centre Potsdam, Telegrafenberg, 14473 Potsdam, Germany

ARTICLE INFO

Keywords:

Thermal diffusivity
Thermal conductivity
Elastic constants
Portlandite $\text{Ca}(\text{OH})_2$
Laser flash method

ABSTRACT

Synthetic portlandite single crystals were used to measure thermal diffusivity and elastic constants. The full tensor of elastic constants c_{ijkl} is derived by Brillouin spectroscopy at ambient conditions. The resultant aggregate bulk and shear moduli are $K_{S, VRH} = 32.2(3)$ GPa and $G_{VRH} = 21.2(2)$ GPa, respectively. The thermal diffusivity D was measured from -100 °C to 700 °C parallel [001] and perpendicular [100] to the crystallographic c -axis using laser flash method. The dehydration of the crystals influences the thermal diffusivity determination depending on sample size, orientation and heating rate. Thermal diffusivity and the derived thermal conductivity show a pronounced anisotropy with a maximum perpendicular to the c -axis, *i.e.* in the plane of the $[\text{CaO}_6]$ octahedral layers. In the same direction the highest sound velocities (v_p and v_{mean}) and longest mean free path length of phonons are determined. The thermal diffusivity as well as the derived thermal conductivity show a distinct temperature dependence.

1. Introduction

Thermoelastic properties such as thermal diffusivity, thermal conductivity, elastic constants as well as dynamic elastic response (*e.g.* sound velocities) are a prerequisite to better understand and predict the behavior of composite materials [1]. The knowledge of thermoelastic properties of portlandite $\text{Ca}(\text{OH})_2$ as one of the major phases (*ca.* 20 wt % [2,3]) in hydrated portland cement based composites is of fundamental importance, affecting the properties of buildings to a great extent [4]. Furthermore, $\text{Ca}(\text{OH})_2$ is used as a reaction medium, especially in the context of numerous process variants for flue gas cleaning in combustion technology [5]. With regard to the further development of these technologies, many studies have addressed the reactivity of portlandite both with SO_2 (*e.g.* [6,7]) and with CO_2 (*e.g.* [8]). Reaction mechanisms and influencing factors are important in view of the variety of technical implementations, which also cover a wide range of temperature conditions [9–11]. It is common practice to assess the reaction kinetics and take into account mineralogical/chemical changes. However, thermal properties resulting from the crystal physics of the relevant compounds, *e.g.* $\text{Ca}(\text{OH})_2$, have not yet been integrated into such

considerations. Beyond that, in the topical field of thermochemical energy storage the reversible dehydration of portlandite is considered as a promising reaction and could play a leading role providing large storage capacities for intermittent renewable energy production in the future [12]. For ongoing numerical and experimental research a detailed knowledge about the thermal transport properties of the reactants is crucial and still lacking particularly for portlandite [13].

Portlandite $\text{Ca}(\text{OH})_2$ is a trigonal hydroxide crystallizing in space group $P\bar{3}m1$ and is isostructural to brucite $\text{Mg}(\text{OH})_2$. The structure is characterized by nearly close-packed oxides forming distorted edge-sharing $[\text{CaO}_6]$ octahedral layers perpendicular to the 3-fold crystallographic c -axis [14–17] (Fig. 1). H is pointing up- and downwards into the interlayer space, expanding the structure in [001] direction. H is displaced from the trigonal symmetry axis and disordered around the 3-fold rotation axis with maximum probability density along the c -axis [16,18]. Whereas ionic bonding is dominant within the $[\text{CaO}_6]$ layers, hydrogen bonds connect the opposing octahedral layers [15,16]. As a result, portlandite shows a perfect cleavage along (001).

Apart from theoretical calculations by Laugesen [20] and Ulian and Valdrè [21], measured full sets of elastic constants c_{ijkl} of portlandite

* Corresponding author.

E-mail addresses: simon.breuer@kit.edu (S. Breuer), matthias.schwotzer@kit.edu (M. Schwotzer), speziale@gfz-potsdam.de (S. Speziale), frank.schilling@kit.edu (F.R. Schilling).

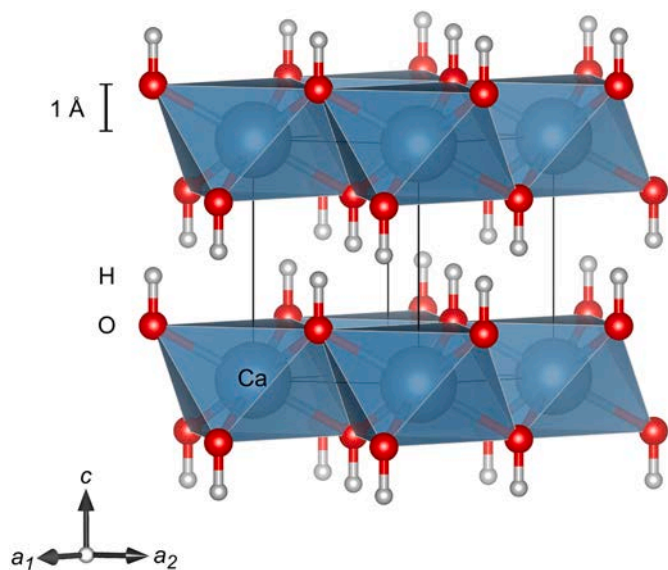


Fig. 1. Crystal structure of portlandite $\text{Ca}(\text{OH})_2$. Edge-sharing $[\text{CaO}_6]$ octahedra (blue, oxygen in red) form layers stacked along the 3-fold c -axis. H atoms (gray) are pointing into the interlayer space and are disordered around the 3-fold axis. Black lines correspond to the edges of one unit cell (drawn using VESTA [19], modified). (For interpretation of the references to colour in this figure legend, the reader is referred to the web version of this article.)

have been reported only by Holuj et al. [22] and Speziale et al. [4]. In contrast, thermal transport properties such as the thermal diffusivity and thermal conductivity seem to be still lacking especially as a function of temperature and in particular for single crystal portlandites. This is most likely due to its rare natural occurrence in general and in particular due to missing single crystals in a sufficient size to perform *e.g.* laser flash measurements.

The aim of this contribution is to enhance our profound knowledge about thermoelastic properties of portlandite with a focus on thermal transport properties. Therefore, large single crystal portlandites were grown by diffusion experiments. These are used to derive the full set of elastic stiffness constants c_{ijkl} by Brillouin scattering experiments at ambient conditions. The results on the elastic behavior of synthetic $\text{Ca}(\text{OH})_2$ crystals are compared to published experimental data on portlandite [4,22]. Thermal transport properties are collected by means of laser flash measurements to derive the thermal diffusivity D in the temperature range from -100 °C over the dehydration temperature of

portlandite up to 700 °C. For the temperature range of portlandite stability from -100 °C to ~ 400 °C, the full set of thermal diffusivity tensor components D_{ij} is obtained. Related thereto, the thermal conductivity tensor components κ_{ij} are derived using tabulated data for isobaric heat capacity and density. Additionally, averaged (Voigt, Reuss, Hill) elastic moduli and thermal diffusivity and thermal conductivity data are also given.

2. Methods

For this study, centimeter-sized portlandite single crystals have been grown and characterized to determine thermal diffusivity and elastic properties while using a laser flash apparatus (LFA) and a Brillouin spectrometer, respectively.

2.1. Samples

Portlandite single crystals were grown by diffusion process proposed by Johnston [23] and adapted by Ashton and Wilson [24] and Johnstone and Glasser [25]. Two plastic bottles (260 ml) were placed ~ 10 cm apart from each other in a large desiccator (DURAN DN250) and deionized water was filled up to a few centimeters over the open top of the bottles (total volume approximately 5 l). One bottle was filled with a 1.6 molal solution of sodium hydroxide (NaOH , $\geq 99\%$), the other bottle with a 0.8 molal solution of calcium chloride (CaCl_2 , $\geq 99\%$) through slow injection (approximately 150–200 ml) at the bottom of the bottles using a syringe. The atmosphere in the sealed, vibration-damped desiccator was pure N_2 . The desiccator was placed in a dark surrounding at a constant temperature $T \approx 23$ °C. The growth of portlandite single crystals took place at the inner rim on the top of the two bottles over several months. Sodium hydroxide and calcium chloride were re-injected 5–8 times (in a 4–6 weeks' interval) into the respective bottles (~ 100 ml solution) whenever no detectable crystal growth was observed over 7–14 days.

For the characterization small parts of the synthesized single crystals were used.

Inductively coupled plasma mass spectroscopy (ICP-MS, X-Series2, Thermo Scientific) was used to determine the content on 22 cations (Table 1, without Ca). Portlandite was pulverized (agate mortar) for acid digestion in HNO_3 (65%, subboiled), HF (40%, suprapur) and HClO_4 (65%, normatom). The accuracy of ICP-MS analysis was tested by the certified standard CRM-TMDW (High Purity Standards).

Contents of carbon and sulfur (Table 1) were measured using a carbon-sulfur-analyzer (CSA) (CS-2000, Eltra). The powdered

Table 1
Elemental composition of synthetic portlandite crystals analyzed by ICP-MS (without Ca), IC and CSA (in ppm wt).

ICP-MS										
Na	Mg	P	K	Ti	Cr	Mn	Fe	Co	Ni	Cu
bdl ^a	23.4(1) ^b	4.0(5)	28.2(7)	0.5(1)	0.2 (1)	1.0(1)	4.2(2)	bdl	0.5(1)	0.1(1)
ICP-MS										
Zn	As	Rb	Sr	Y	Mo	Ag	Cd	Ba	Pb	
1.0(2)	1.5(1)	bdl	bdl	bdl	0.1(1)	0.1(1)	bdl	bdl	bdl	bdl
IC								CSA		
F^-	Cl^-	Br^-	$(\text{NO}_3)^-$	$(\text{PO}_4)^{3-}$	$(\text{SO}_4)^{2-}$	C	S			
bdl	481(2)	bdl	81(3)	bdl	208(2)	511(5)	7.0(1)			

^a bdl below detection limit (Na: 3 ppm, others: ≤ 0.1 ppm).

^b Numbers in parentheses are 1σ standard deviation of the last digits.

portlandite (~150 mg) was heated to $T \approx 2000$ °C. A fragment of the steel chip reference standard 92400-3050 (Eltra) was used for accuracy evaluation.

Anions were analyzed using an ion chromatography (IC) system (ICS-1000, Dionex) (Table 1). Fine powdered $\text{Ca}(\text{OH})_2$ ($m = 115.3$ mg) was mixed with 10 ml deionized water for ~5 min before filtering and instantaneously measuring the solution. The certified reference material CRM-LGC6020 (river anions, LGC Standards) was used for accuracy validation.

Thermogravimetric (TG) analysis was carried out using a TGA 2 (Mettler Toledo) system (Fig. 10b). A powdered $\text{Ca}(\text{OH})_2$ sample ($m = 37.6$ mg) was placed in an aluminum oxide crucible and the mass loss was recorded at a heating rate (HR) of 5 K/min over the temperature range from 30 °C to 1000 °C under N_2 atmosphere (99.99%).

For differential scanning calorimetry (DSC) plane single crystal platelets (001) were placed in aluminum pans (empty reference pan) in a DSC apparatus DSC822e (Mettler Toledo). Two independent measurements were carried out under N_2 atmosphere (99.99%) at different temperature ranges and heating rates (Fig. 10b): 1) T from -100 °C to 550 °C (liquid N_2 cooled, HR 10 K/min, specimen cross section ~3.3 mm, ~0.5 mm thick, $m \approx 8.0$ mg) and 2) T from 300 °C to 575 °C at a reduced heating rate of 2 K/min (~3.6 mm cross section, ~0.5 mm thickness, $m \approx 9.5$ mg).

Powder X-ray diffraction (XRD) measurements (D8 Discover, Bruker) (Fig. 2) were carried out on portlandite as well as on the dehydration product directly after performing laser flash measurements. Patterns were taken from 10° to 80° (2θ) in steps of 0.02° with incident $\text{Cu K}\alpha$ radiation (40 kV, 40 mA).

The grown $\text{Ca}(\text{OH})_2$ single crystals are transparent and free of visible inclusions or foreign phases under the light microscope. The crystals are idiomorphic/hypidiomorphic and exhibit elongated (along crystallographic c -axis) pseudo-hexagonal prisms of up to 1.5 cm length and ~7 mm in cross section, respectively. The elemental composition is presented in Table 1. No significant changes in element concentrations for single crystals originating in different batches were found nor could any spatial variation in composition (mineral zoning) be detected by sampling different states of growth. Except for carbon, chlorine, sulfate and nitrate (all $\leq 0.05\%$), foreign ion contents are in the low ppm range.

The results of the powder XRD measurements are shown in Fig. 2. The diffraction pattern solely shows portlandite reflections for the measured powdered single crystal. After high temperature LFA measurements were carried out, the XRD pattern of the powdered sample shows mainly reflections of CaO , *i.e.* the dehydration product of portlandite (gray, Fig. 2). Only few portlandite reflections are present, *e.g.* at $2\theta \sim 18^\circ$ (001), $2\theta \sim 34^\circ$ {101} and $2\theta \sim 64^\circ$ ($2\bar{1}2$) and {103} and low in intensity. The pattern of the dehydrated portlandite shows

significant bigger full widths at half maximum (FWHM) compared to the pre-heated portlandite powder XRD. As during LFA measurements the temperatures reached 700 °C, it is evident that portlandite single crystals completely dehydrate. Thus, $\text{Ca}(\text{OH})_2$ reflections in the post-heated specimen (gray, Fig. 2) are most likely originating from a rehydration of CaO [26]. The unit cell parameters of the synthesized portlandite crystals determined by Rietveld refinement (Topas, Bruker) are $a_1 = 3.594(1)$ Å, $c = 4.910(1)$ Å, $V = 54.93(3)$ Å³ ($T = 20$ °C) and the thereof calculated density is $\rho = 2.240(2)$ g/cm³, all of which are well in agreement to published data, *e.g.* [4,17,27].

2.2. Brillouin scattering

Acoustic wave velocities and hence elastic properties of samples can be derived by Brillouin scattering using inelastic scattering of light by thermally activated vibrations (phonons) [28–30]. For transparent single crystal specimens the full elastic (stiffness) tensor c_{ijkl} can be resolved. For a detailed review on Brillouin scattering see, *e.g.*, Vacher and Boyer [31] and Speziale et al. [32].

For the experiments in this study the incident light for scattering was produced by a solid state Nd:YVO₄ laser (Verdi Series, Coherent) emitting at $\lambda_0 = 532.15$ nm with a power of approximately 100 mW. With the use of a symmetric forward scattering geometry, knowledge of the refractive index of the specimen is not required [33]. The external (outside of the specimen) scattering angle (angle between the incoming and scattered beam) was set to $\phi = 60^\circ$. Scattered light was analyzed by a six-pass tandem Fabry-Perot interferometer (TFP-1, JRS Scientific Instruments) [34]. The interferometer mirror spacing was set to 10 mm, corresponding to a spectral range of 14.99 GHz. The finesse is ~75. A solid state single-photon counter tube (Count-10B, Laser Components) with low dark counts and high quantum efficiency > 65% (at 532 nm) was used to detect the signal. A simplified schematic construction of the Brillouin scattering experimental setup is shown in Fig. 3.

For Brillouin scattering experiments two single crystal orientations have been prepared. One platelet parallel to the perfect cleavage along (001) (so-called “basal”) and one platelet in perpendicular direction (100), referred to as “axial”. The opposing crystal faces have been ground and polished to plane-parallelism (deviation < 1.0°) down to 1 μm grit size. The specimens were attached to a thin polycrystalline diamond platelet on a goniometer head and set in the center of the Eulerian cradle (Fig. 3) in the focus of the incident laser beam.

Inelastic scattering of light manifests in a Doppler shift in frequency [36], which results in a spectrum symmetric to the unshifted line (Fig. 4). The frequency shifts $\Delta\omega$ in Brillouin spectra are linked to the acoustic sound velocities v (*e.g.* [33]):

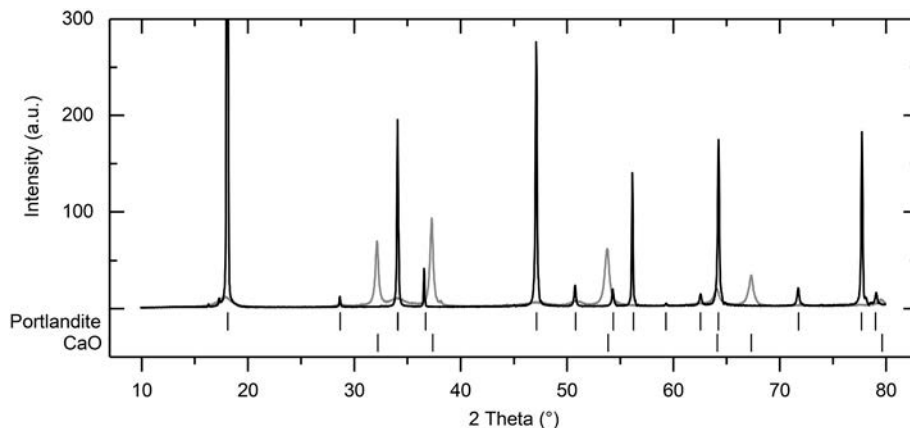


Fig. 2. X-ray diffraction on powdered portlandite (black) and its dehydration product (gray) after thermal diffusivity measurements were carried out up to $T = 700$ °C (phase identification: portlandite - ICDD PDF 04-0733, CaO - ICDD PDF 04-0777).

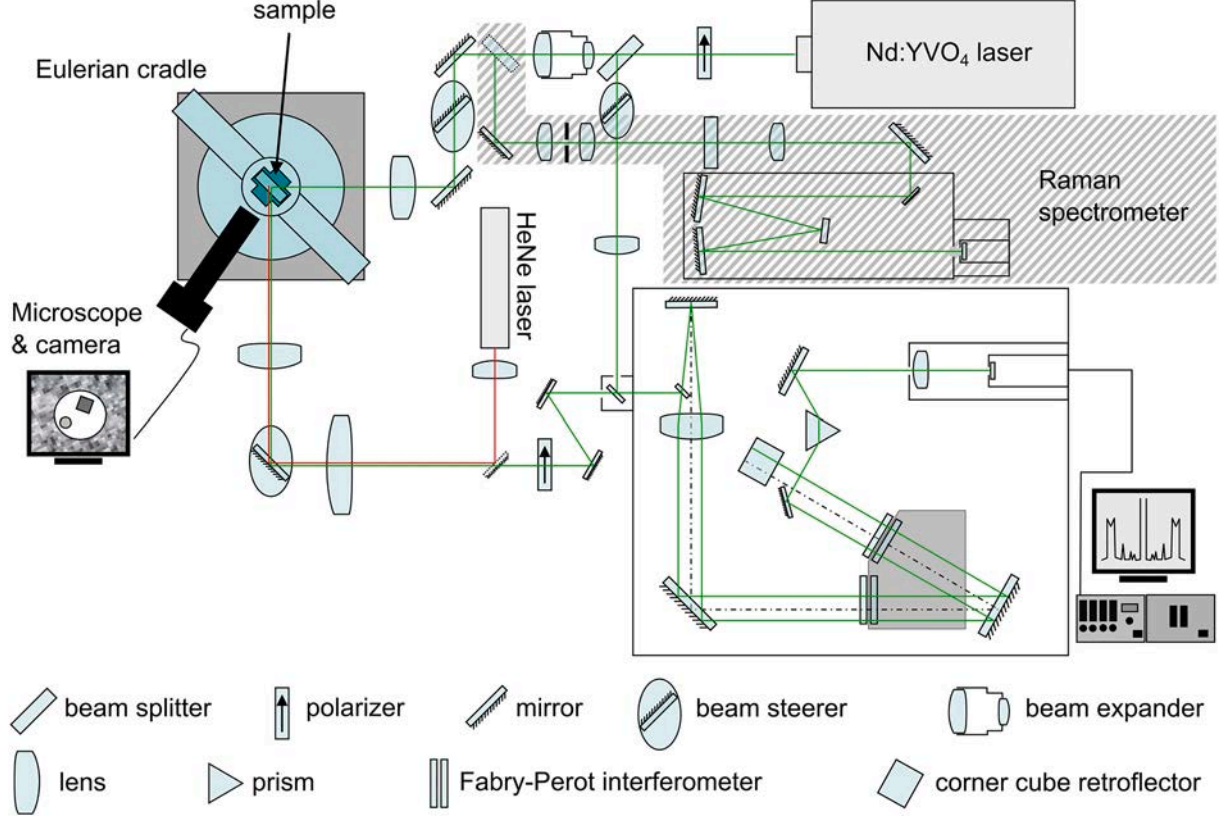


Fig. 3. Schematic diagram of the experimental setup used for Brillouin scattering with attached Raman spectrometer (hatched gray). The HeNe laser is used for sample placement and alignment of the experimental setup (modified after Speziale and Duffy [35]).

$$v_{p,s} = \frac{\Delta\omega_{p,s}\lambda_0}{2\sin(\phi/2)} \quad (1)$$

with incident wavelength λ_0 , external scattering angle ϕ and subscripts p and s denote the quasi-longitudinal and quasi-transverse acoustic modes, respectively. For ideal elastic bodies (Hooke's law behavior) the relation of acoustic wave velocities and stiffness tensor c_{ijkl} is described by an equation of motion (atomic displacements). The solution for plane waves is given by the Christoffel's equation [37,38]

$$(\Gamma_{ij} - \rho v^2 \delta_{ij})u_j = 0 \quad (2)$$

with the Christoffel matrix $\Gamma_{ij} = c_{ijkl}n_j n_l$, where n_j and n_l are the direction cosines of the phonon propagation vector, ρv^2 is the eigenvalue (with ρ the density and v the wave velocity), u_j gives the polarization of the corresponding phonon (eigenvector), and δ_{ij} is the Kronecker delta. 36 directions have been measured on each of two different specimen platelets. The elastic tensor of portlandite consists of a total of six independent coefficients (e.g. [39]). The Christoffel's equation is thus over-determined and solved for c_{ijkl} using an inhouse software with least-square Levenberg-Marquardt algorithm [40,41]. Together with the fit of the components of the stiffness tensor c_{ijkl} , the crystallographic orientations of used specimen platelets were refined as well. For the data evaluation, portlandite has been treated as optically isotropic material (birefringence $\delta_{max} = 0.027$ [22,42]). The errors involved with this simplification are small and well within the reproducibility of the experiment [4,43].

Periodically repeated single-crystal MgO measurements at ambient conditions over a period of several years yield to a reproducibility of $\sim 0.5\%$ for the used setup while the accuracy is $\sim 1.0\%$.

2.3. Thermal diffusivity

Measurements on lattice thermal diffusivity D of single crystal

portlandite have been carried out by transient laser flash method [44] using a Netzsch MicroFlash LFA 457 system. A short duration laser pulse heats up the front of a plate-like specimen and the resulting time-dependent temperature change is recorded on the opposite back side. A brief overview of the method is given by, e.g., Vozár and Hohenauer [45].

The radiant source used for the measurements is a Nd:YAG laser emitting at 1064 nm (IR Sources Inc.). It produces a short duration (~ 0.3 ms) 0.5" enlarged pulse with a maximum power output of 18.5 J, operated at approximately 4 J. The specimens were placed inside a furnace continuously flushed with N_2 purge gas (99.99%, 50 ml/min). For the placement of the specimens inside the furnace custom ceramic sample holders were made of Macor glass ceramic (Schröder Spezialglas). The temperatures were measured close to the specimens using a type K thermocouple (class 1, DIN EN/IEC 60584-1 [46]). For measurements at low temperatures (-100 °C to 100 °C) a HgCdTe (MCT) infrared (IR) detector was installed, for measurements from ambient conditions up to $T = 700$ °C an InSb detector was used. To reduce a possible laser profile non-uniformity, a custom 1" laser homogenizer (RD 203, Holo/Or Ltd.) was installed beneath the sample for the low temperature setup. The heating rate (HR) between each temperature step was set to 3 K/min and the specimens were held for ~ 0.5 h at each temperature step. The temperature increase of the specimens is approximated to be $\Delta T \leq 1$ K within each measurement. The IR detector output is assumed to be linear to the temperature and the thermophysical properties and density ρ of $Ca(OH)_2$ are assumed to be constant within ΔT of each independent measurement at a pre-defined temperature. A schematic diagram of the used laser flash setup for thermal diffusivity measurements is shown in Fig. 5.

For the LFA experiments five basal (D measured along [001]) and six axial ($D \perp c$ -axis) portlandite platelets have been prepared. A total of over 1100 independent thermal diffusivity measurements were

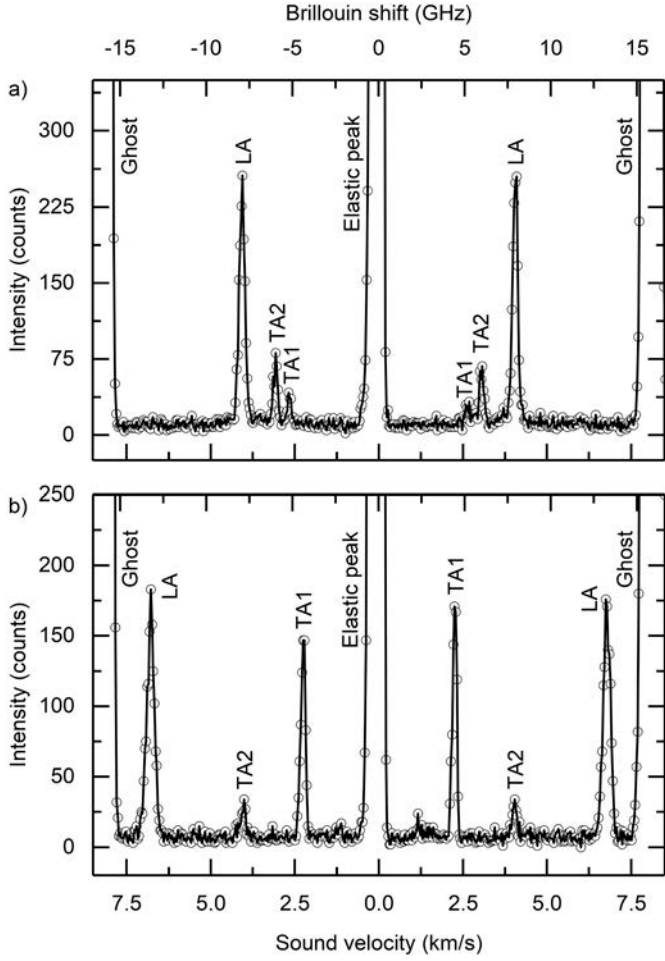


Fig. 4. Brillouin spectra of portlandite a) in the axial plane (100) and b) in perpendicular direction (001) (basal plane). LA: quasi-longitudinal acoustic wave (v_p), TA1 and TA2: slow (v_{s2}) and fast (v_{s1}) quasi-transverse acoustic wave. Ghost peaks correspond to higher order elastically scattered incident light.

performed for axial or basal orientations. Reported thermal diffusivities are an average of at least three independent measurements at the corresponding temperature per specimen and the mean of five basal and six axial platelets, respectively. The crystallographic orientations of the axial platelets have been determined by single crystal X-ray diffraction (SC-XRD, D8 Quest, Bruker, Mo K_α microfocus source $I\mu S$ 3.0, 50 kV, 1.4 mA) while the basal specimens perfectly cleaved in (001) platelets. The out-of-plane angles of the principal crystallographic axial plane orientations (100) are less than 1.0° for all specimens. This misorientation of the specimens for LFA measurements led to a systematic error of $\leq 0.05\%$ for the thermal diffusivity D values, far below the reproducibility of the laser flash apparatus and is therefore neglected for the description of the thermal diffusivity D_{ij} and thermal conductivity κ_{ij} tensor. All specimens have been ground to plane-parallelism (deviation $< 1^\circ$) and the surfaces were slightly roughened for a better adhesion of the coatings and to attenuate a possible non-uniformity of the laser [48]. $\text{Ca}(\text{OH})_2$ platelets as well as the sample holders were sputter-coated with Au (99.99%) to $\sim 0.1 \mu\text{m}$ (108 manual, Cressington) to reduce a direct radiative heat transfer. The specimens were additionally coated with graphite spray (Graphit 33, CRC Industries) to $\sim 10 \mu\text{m}$ thickness per side to achieve a uniform and consistent laser pulse absorption [49,50]. The thicknesses d reached from 0.5 mm to 1.3 mm for the basal cut and from 1.0 mm to 1.7 mm for the axial orientation. The cross sections varied from 3 mm to 7 mm. Thicknesses were corrected according to linear thermal expansion

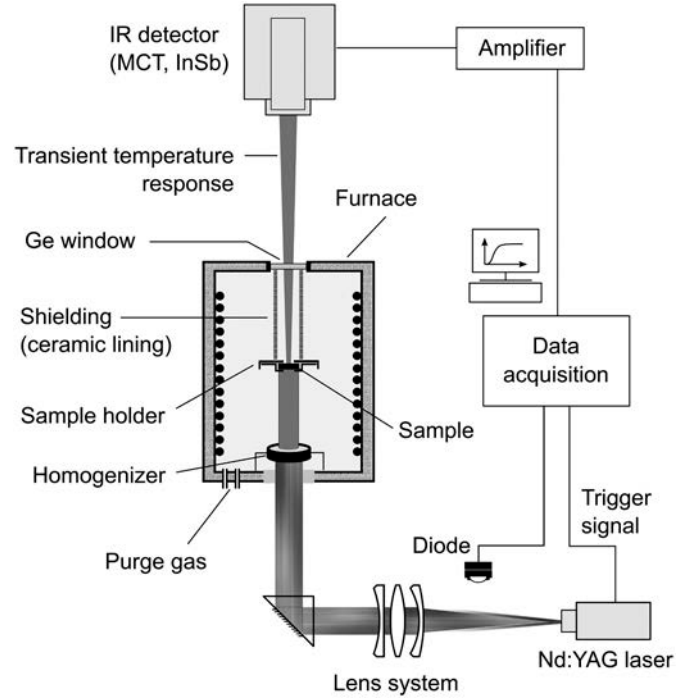


Fig. 5. Schematic diagram of the used laser flash apparatus for measurements of thermal diffusivity. (Adapted after Breuer and Schilling [47]).

coefficients given by Xu et al. [51] for portlandite (extrapolated from 35°C to -100°C and from 370°C to 520°C) and by Fiquet et al. [52] for CaO . For the transition region $T = 450\text{--}520^\circ\text{C}$ an altering linear mixture of both expansion coefficients was applied.

According to Fourier's law, one-dimensional conductive heat flow is described by

$$q = -\kappa \frac{\partial T}{\partial x} \quad (3)$$

with heat flux q , constant temperature gradient $-\partial T/\partial x$ and thermal conductivity κ (2nd rank tensor for anisotropic solids). The temperature equilibration in a homogeneous solid is described by [53].

$$\frac{\partial T}{\partial t} = D \frac{\partial^2 T}{\partial x^2} \quad (4)$$

With known lattice thermal diffusivity D of a solid, the thermal conductivity κ can be derived using the isobaric heat capacity c_p and density ρ :

$$\kappa = D\rho c_p \quad (5)$$

For thermal diffusivity measurements by the laser flash method a short-duration heat pulse is absorbed by the specimen's front surface and the resulting temperature change over time t at the back side is given as [44]

$$T(d, t) = \frac{Q}{\rho c_p d} \left[1 + 2 \sum_{n=1}^{\infty} (-1)^n \exp\left(\frac{-n^2 \pi^2 D t}{d^2}\right) \right] \quad (6)$$

assuming adiabatic conditions, with Q the heat pulse energy absorbed and the specimen thickness d . The evaluation of the thermal diffusivity D is performed by an inhouse software using least-square Levenberg-Marquardt algorithm on the basis of Eq. (6) including a custom heat loss model and a finite pulse-time correction (for details, see Breuer and Schilling [47]) (Fig. 6). The temperature-time history was fitted to $4\text{--}8 \times t_{1/2}$ (with $t_{1/2} = 0.1388 d^2/D$ [44]). The reproducibility of the laser flash thermal diffusivity measurements is $\sim 2\text{--}3\%$. The accuracy was tested in the corresponding temperature range using standard samples

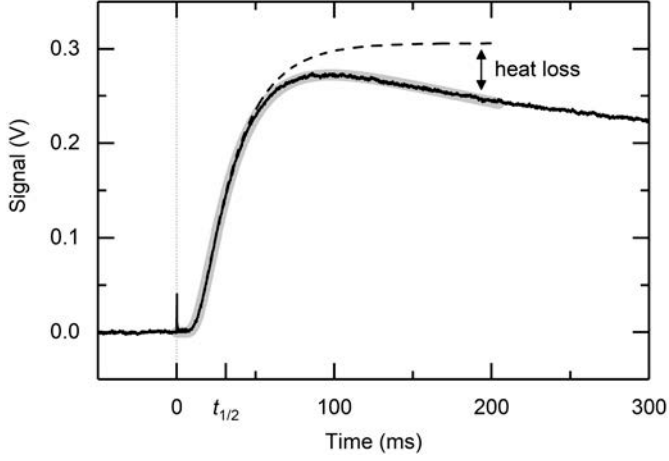


Fig. 6. Signal-time curve (solid black) of portlandite (basal plane, $d = 0.505(3)$ mm) measured by the laser flash method with the low temperature setup (MCT IR detector) at $T = -60.5$ °C. The adiabatic temperature evolution (cf. Eq. (6)) is shown as dashed black line, the approximated curve including finite pulse-time correction and heat loss to the surroundings is shown as thick gray line. The dotted vertical line (gray) corresponds to the release of the laser pulse used to heat up the front surface of the specimen. The time at half maximum is given as $t_{1/2} = 0.1388 d^2/D$.

(Pyroceram 9606, Inconel 600, Stainless Steel 310) and is $\sim 5\%$.

Comparable to the calculation of aggregate elastic moduli, the 2nd rank thermal diffusivity tensor D_{ij} (and similarly κ_{ij}) may be averaged in a Voigt- [54] and Reuss-like [55] behavior as

$$D_V = \frac{1}{3} \sum_{i=1}^3 D_{ii} \quad (7)$$

and

$$\frac{1}{D_R} = \frac{1}{3} \sum_{i=1}^3 \frac{1}{D_{ii}} \quad (8)$$

The Voigt-Reuss-Hill [56] average is determined as the arithmetic mean of D_V and D_R .

3. Results

3.1. Brillouin scattering

The acoustic wave velocities determined in axial and basal planes are shown in Fig. 7. The refined specimen orientations, given as rotation axes of the surface normal of the platelets, are $89.3^\circ/89.1^\circ$ (azimuth/pole distance) for the axial plane and $-9.6^\circ/1.1^\circ$ for the basal plane, respectively. This includes both sample preparation and sample mounting on the goniometer head. Standard deviations 1σ of the refined orientations are $\sim 1.0^\circ$. The elastic constants have been approximated by applying Eq. (2) to a total of 216 determined quasi-longitudinal or quasi-transverse acoustic wave velocities in the axial or basal plane orientation. The resultant components of the stiffness tensor C_{ij} (Voigt notation) are given in Table 2. Using these, the calculated velocities (black lines) fitted to the measured data (circles) are shown in Fig. 7. The acoustic wave velocities show a distinct anisotropy between the crystallographic c -axis (*i.e.* [001]) and a_1 -axis ($= a_2 = a_3, \langle 100 \rangle$). The highest velocities and a maximum shear wave splitting are measured in directions perpendicular to the c -axis with $v_p = 6.8(1)$ km/s, $v_{S1} = 4.0(1)$ km/s and $v_{S2} = 2.3(1)$ km/s. The variations of acoustic velocities within the $a_1 - a_2 - a_3$ plane (001) are < 15 m/s and show a sixfold symmetry.

Representing surfaces for the acoustic wave velocities and for the Young's modulus (*e.g.* see Nye [39]) are shown in Figs. 8a, c, e and 9a,

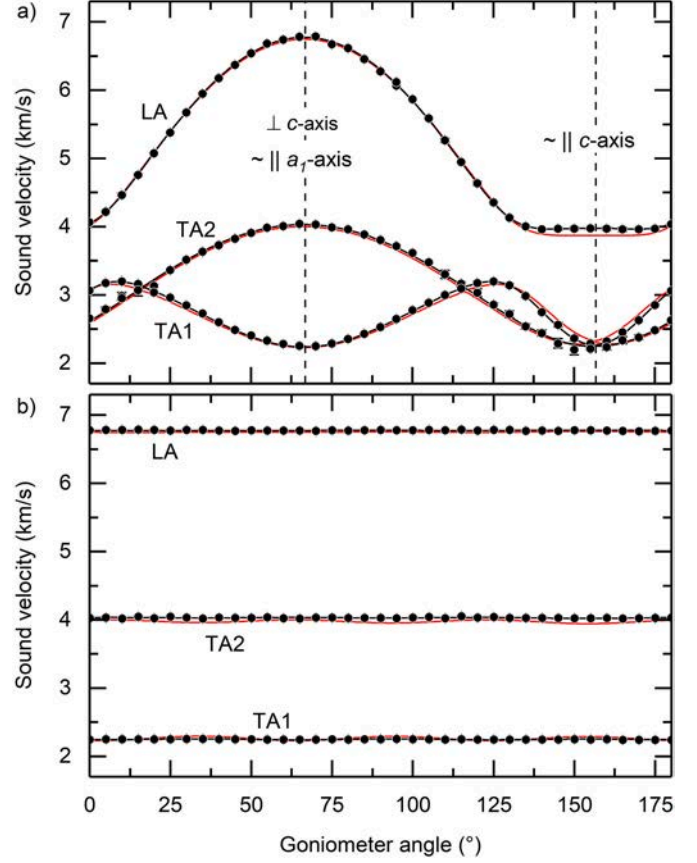


Fig. 7. Measured (circles) acoustic wave velocities of synthetic single crystal portlandite in a) axial plane and b) basal plane. Solid black lines correspond to calculated velocities based on the elastic constants determined in this study (Eq. (2)). Red solid lines correspond to calculated acoustic velocities using the elastic constants of natural portlandite determined by Speziale et al. [4] (cf. Table 2). LA: quasi-longitudinal acoustic wave (v_p), TA1 and TA2: slow (v_{S2}) and fast (v_{S1}) quasi-transverse acoustic wave, respectively. (For interpretation of the references to colour in this figure legend, the reader is referred to the web version of this article.)

Table 2

Synthetic portlandite single crystal elastic constants C_{ij} (Voigt notation) derived by Brillouin spectroscopy at ambient conditions. For comparison, literature data on synthetic and natural $\text{Ca}(\text{OH})_2$ are shown. Components in GPa.

	Speziale et al. [4]	Holuji et al. [22]	This study
	(Natural $\text{Ca}(\text{OH})_2$)	(Synthetic $\text{Ca}(\text{OH})_2$)	
C_{11}	102.0(20)	99.3(15)	102.8(8)
C_{12}	32.0(10)	36.2(20)	30.2(5)
C_{13}	8.4(4)	29.7(150)	8.9(5)
C_{14}	4.5(2)	0 ^a	2.1(4)
C_{33}	33.6(7)	32.6(20)	35.4(4)
C_{44}	12.0(3)	9.8(20)	11.4(2)
C_{66} ^b	35.0(11)	31.6(15)	36.3(5)

^a Assumed.

^b $C_{66} = (C_{11} - C_{12})/2$.

respectively. They show well the trigonal symmetry of portlandite. Selected cuts are shown on the right hand side of Figs. 8 & 9: azimuth = 30° (black) crossing the minimum and opposing maximum (rotoinversion) of the corresponding property and the basal plane (001) (gray). The anisotropic Young's modulus E shows a large variation with $E_{max}/E_{min} \sim 3$. It is smallest at a pole angle of $145^\circ/325^\circ$ (azimuth = 30°) with $E_{min} = 29.6(2)$ GPa (Fig. 9b). The Young's modulus features a small local maximum $E_{[001]} = 34.3(2)$ GPa perpendicular to

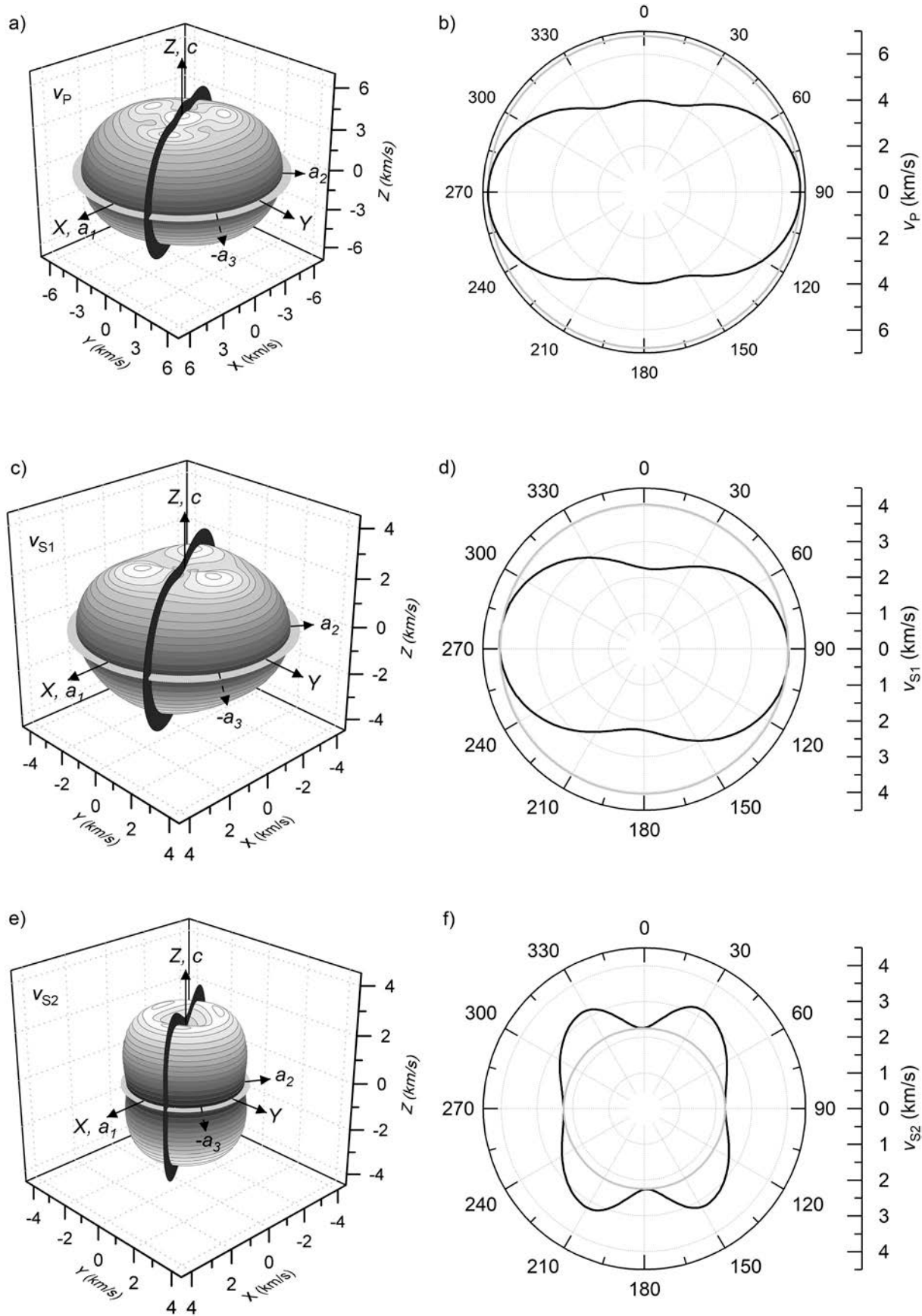


Fig. 8. 3D representation of the acoustic wave velocities v_p (a), v_{s1} (c) and v_{s2} (e) of portlandite. Two selected cuts, azimuth = 30° (black) and basal plane (001) (gray), are shown in b), d) and f).

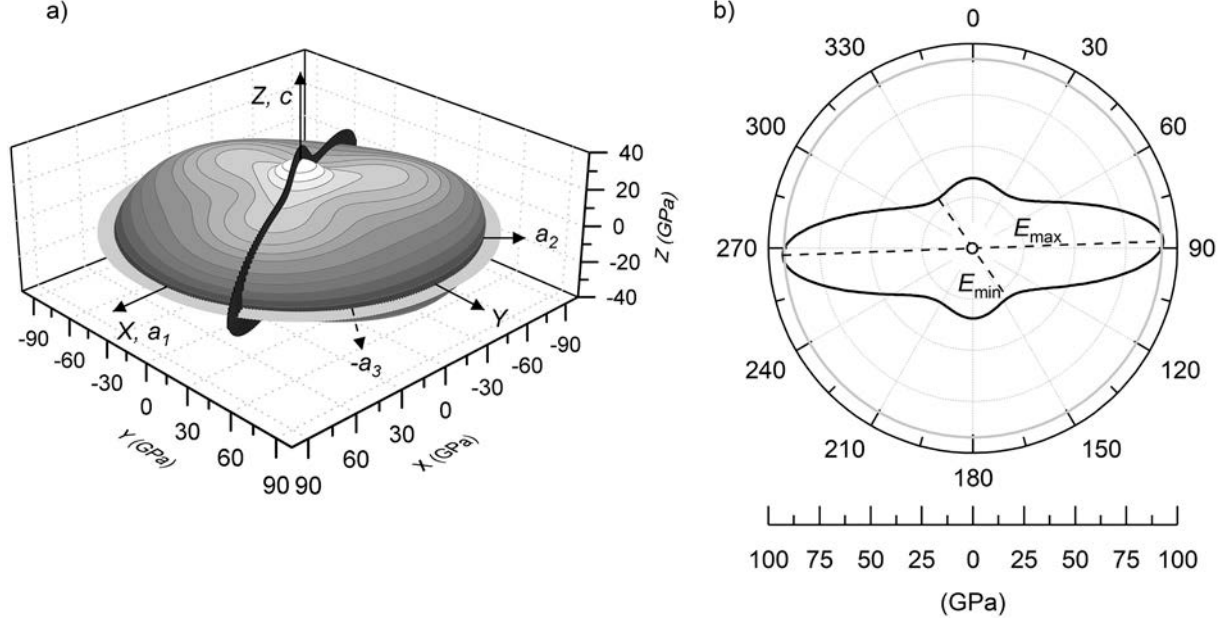


Fig. 9. Young's modulus E of synthetic portlandite as three-dimensional representation (a) and b) two selected cuts along azimuth = 30° (black) with E_{min} and E_{max} and the basal plane (001) (gray).

the layered structure of $\text{Ca}(\text{OH})_2$, *i.e.* in c -axis direction. Its overall maximum lies at a pole angle $88^\circ/268^\circ$ (azimuth = 30°) with $E_{max} = 93.1(4)$ GPa (Fig. 9b). In the basal plane (pole = 90°) the Young's modulus is slightly reduced with $E_{[100]} = 92.2(3)$ GPa.

The adiabatic aggregate elastic moduli and velocities for an isotropic polycrystalline material calculated on the basis of the measured C_{ij} for synthetic $\text{Ca}(\text{OH})_2$ are shown in Table 3 together with the elastic moduli calculated for natural portlandite after Speziale et al. [4]. Except for the Reuss bound adiabatic bulk modulus (K_S, R), differences of the aggregate elastic moduli and velocities for synthetic and natural portlandite are $\leq 2\%$.

Table 3

Adiabatic aggregate elastic moduli and acoustic velocities for portlandite at ambient conditions. Elastic moduli K_S, G, E in GPa, wave velocities v in km/s.

	Speziale et al. [4] (Natural $\text{Ca}(\text{OH})_2$)	This study (Synthetic $\text{Ca}(\text{OH})_2$)
K_S, v	37.3(4)	37.4(3)
K_S, R	26.0(3)	27.0(3)
K_S, VRH	31.6(3)	32.2(3)
G_V	24.4(3)	24.7(2)
G_R	17.5(4)	17.7(2)
G_{VRH}	20.9(3)	21.2(2)
E_V	60.0(8)	60.7(5)
E_R	42.8(10)	43.6(4)
E_{VRH}	51.4(10)	52.2(4)
ν_V	0.23(1)	0.23(1)
ν_R	0.23(1)	0.23(1)
ν_{VRH}	0.23(2)	0.23(1)
ν_P, VRH	5.15(2)	5.20(2)
ν_S, VRH	3.05(2)	3.08(1)
$\nu_{mean, [001]}$	2.93(2)	2.95(1)
$\nu_{mean, [100]}$	4.71(2)	4.73(2)

V Voigt [54], R Reuss [55] and VRH Voigt-Reuss-Hill [56] average elastic moduli (*e.g.* [57,58]).

ν Poisson's ratio.

$$\nu_P, VRH = K_S, VRH + 4/3G_{VRH} \text{ and } \nu_S, VRH = \sqrt{G_{VRH}/\rho}.$$

$$\nu_{mean} = \sqrt{(v_P^2 + v_{S1}^2 + v_{S2}^2)/3}, [59].$$

3.2. Thermal diffusivity and thermal conductivity

The results of laser flash thermal diffusivity D measurements on synthetic single crystal portlandites in basal (*i.e.* D along [001], tensor component D_{33}) and axial plane ($D \perp c$ -axis, D_{11}) orientations are presented in Fig. 10 (tabulated values see Appendix A) together with the results of TG and DSC measurements.

The thermal diffusivity decreases with increasing temperature over the entire portlandite stability field for both directions investigated. The temperature diffuses much faster in the plane of the $[\text{CaO}_6]$ octahedral layers $\perp c$ -axis ($D_{11} = D_{22} = 6.1(2)$ mm^2/s at 25°C) than parallel to the c -axis ($D_{33} = 0.73(2)$ mm^2/s). The pronounced anisotropy of thermal diffusivity can be calculated as $D_{[100]}/D_{[001]}$ and is shown in Fig. 11 up to the beginning of the dehydration of portlandite. At $T = -100^\circ\text{C}$ the thermal diffusivity is almost ten times higher in [100] (axial plane) than in the perpendicular [001] direction (basal plane). The anisotropy gradually reduces to $D_{[100]}/D_{[001]} \sim 8.3(3)$ at ambient conditions and stays roughly constant up to the beginning dehydration.

With the components of D_{ij} measured by laser flash method, the Voigt- (Eq. (7)) and Reuss-like (Eq. (8)) averaged thermal diffusivities for single crystal portlandite are shown in Fig. 10a together with the Voigt-Reuss-Hill average. At ambient conditions it is: $D_V = 4.31(13)$ mm^2/s , $D_R = 1.78(3)$ mm^2/s and $D_{VRH} = 3.04(7)$ mm^2/s . However, due to the layered structure of $\text{Ca}(\text{OH})_2$ it is worth mentioning that an actual bulk thermal diffusivity of a general polycrystalline aggregate of portlandite is strongly depending on the texture [61] and porosity [62].

Regarding the DSC curves in Fig. 10b, no significant heat flow can be seen for the low temperature measurement starting at $T = -100^\circ\text{C}$ (dashed gray, shown up to 300°C , HR 10 K/min). Above room temperature, one reaction can be identified for both TG (black) and DSC (solid gray, HR 2 K/min) curves, *i.e.* the dehydration of $\text{Ca}(\text{OH})_2$ to CaO (*cf.* Fig. 2). For the selected experimental conditions, the release of H_2O takes place from 386°C to 514°C . The TG measurement on powdered $\text{Ca}(\text{OH})_2$ shows a total mass loss of ~ 23.6 wt% for the dehydration reaction while the DSC characterizes this dehydration as endothermic reaction (Fig. 10b).

With respect to the measured thermal diffusivity in this temperature range, a further distinct decrease of nearly 40% for both directions [100] and [001] is shown. Above 514°C , thermal diffusivity stays roughly constant at $D_{[001]} \approx 0.15(1)$ mm^2/s and $D_{[100]} \approx 1.32(5)$ mm^2/s .

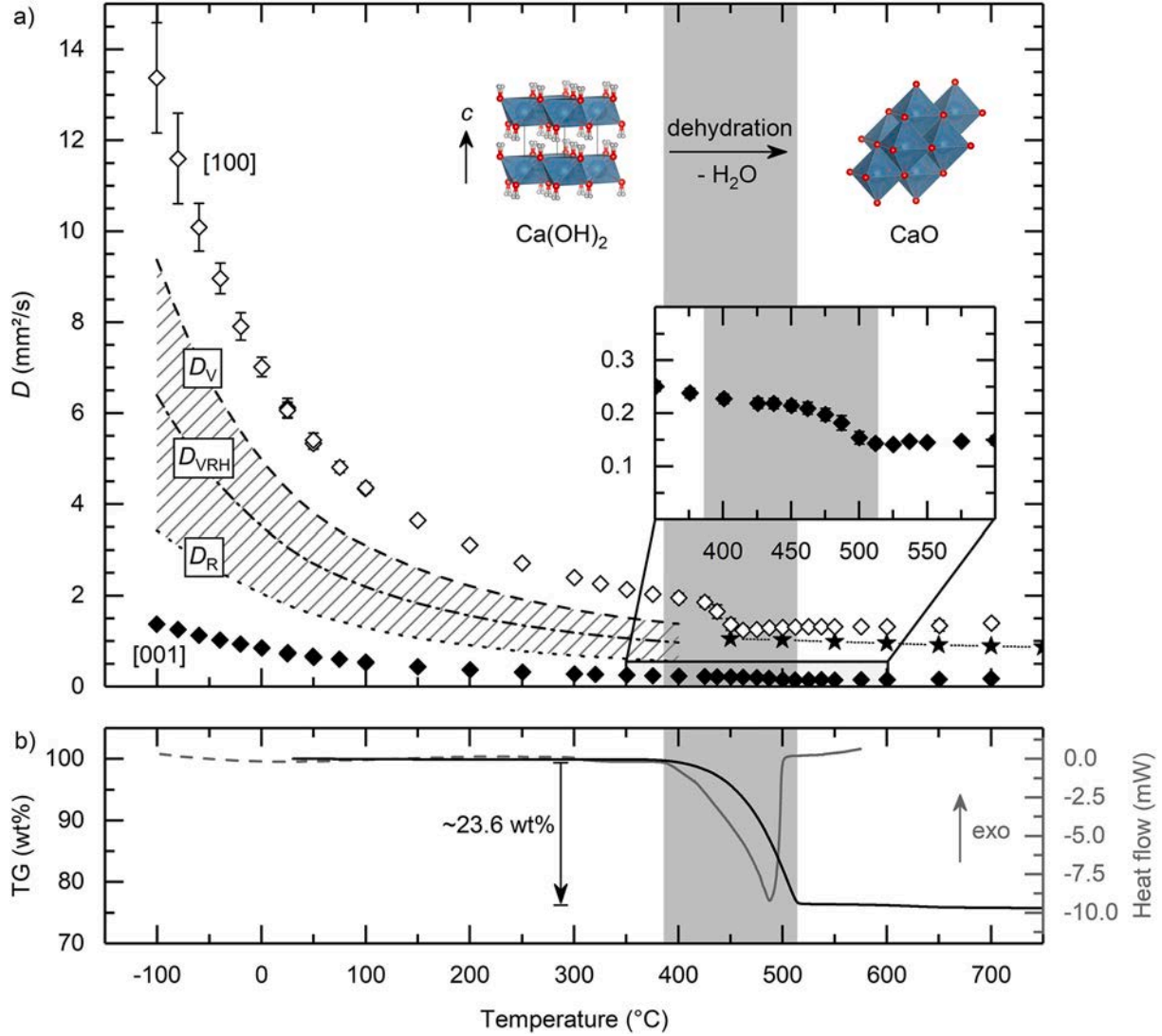


Fig. 10. a) Thermal diffusivity measured by laser flash method for synthetic single crystal portlandite in [001] (basal plane, solid diamonds, $=D_{33}$) and [100] direction (axial plane, open diamonds, $=D_{11}$) from -100 °C through the dehydration of portlandite (gray shaded) to 700 °C. D_V and D_R correspond to Voigt- and Reuss-like averaged thermal diffusivities, D_{VRH} denotes the Voigt-Reuss-Hill average. Stars correspond to thermal diffusivity measurements of burnt lime (CaO) by Yur'ev and Spirin [60]. b) Results of thermogravimetric (TG, black) and differential scanning calorimetric (DSC, gray) measurements on $\text{Ca}(\text{OH})_2$. For details, see text.

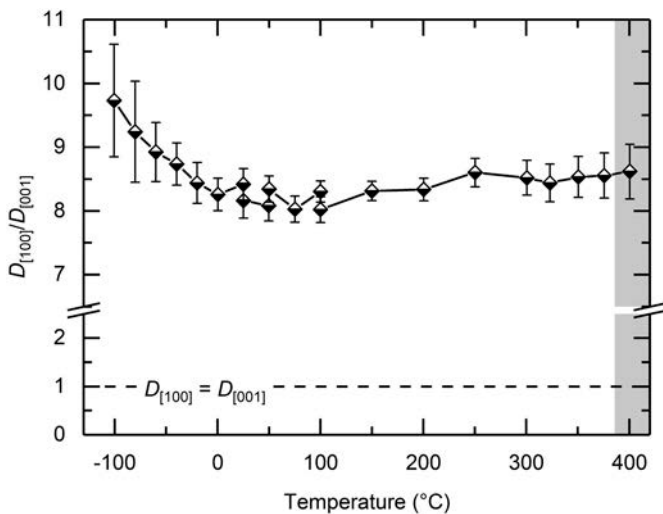


Fig. 11. Anisotropy of the thermal diffusivity D_{100}/D_{001} of synthetic single crystal portlandite.

s. Thus, the thermal diffusivities of CaO from dehydrated $\text{Ca}(\text{OH})_2$ single crystal platelets exhibit an anisotropy and lie above ([100]) and below ([001]) the measured D values for CaO after decarbonation of polycrystalline limestone ($D \sim 0.95$ mm²/s, stars in Fig. 10a, [60]). An apparent slight trend to increasing D values for high temperatures $T > 550$ °C might be caused by the degradation of sputtered Au on the sample holders, which resulted in an increasing transparency of the used ceramic.

The thermal conductivity κ for single crystal portlandite is derived according to Eq. (5) using the thermal diffusivities measured by laser flash method (this study, Fig. 10a). The density is $\rho = 2.240(2)$ g/cm³ (20 °C, see Section 2.1) and adjusted in consideration of the thermal expansion coefficients given by Xu et al. [51]. For the isobaric heat capacity, tabulated quantities according to Chase [63] (based on Kobayashi 1950 (cited by [63]) and Hatton et al. [64]) are used. The resulting tensor components κ_{11} and κ_{33} (tabulated values see Appendix B) together with averaged thermal conductivities (cf. Eqs. (7) & (8)) are shown in Fig. 12. The thermal conductivity is decreasing over the whole temperature range. For temperatures above room temperature, a trend roughly proportional to $1/T$ (Eucken's law [65]) can be recognized while for temperatures below 25 °C the slope of $\kappa(T)$ decreases slightly.

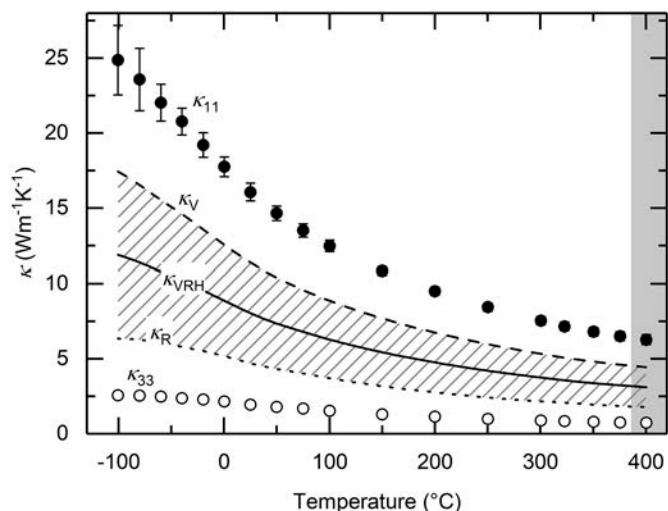


Fig. 12. Derived thermal conductivity κ of portlandite (Eq. (5)): tensor components κ_{11} (\perp c -axis, solid circles) and κ_{33} (\parallel c -axis, open circles) and Voigt and Reuss-like averaged quantities with the Voigt-Reuss-Hill average (κ_{VRH}) (Eqs. (7) & (8)).

Comparable to the thermal diffusivity, heat diffuses ~ 8 – 10 times more effectively perpendicular to the 3-fold c -axis than parallel along $[001]$. At ambient conditions, the 2nd rank thermal conductivity tensor components for single crystal portlandite are $\kappa_{11} = 16.1(6) \text{ Wm}^{-1}\text{K}^{-1}$ and $\kappa_{33} = 1.94(6) \text{ Wm}^{-1}\text{K}^{-1}$. The averaged thermal conductivities at 25°C are $\kappa_V = 11.4(4) \text{ Wm}^{-1}\text{K}^{-1}$, $\kappa_R = 4.69(13) \text{ Wm}^{-1}\text{K}^{-1}$ and $\kappa_{VRH} = 8.02(25) \text{ Wm}^{-1}\text{K}^{-1}$, respectively. As noted with respect to the thermal diffusivity, the effective thermal conductivity of a bulk of polycrystalline portlandite strongly depends on its texture and porosity.

4. Discussion

The spatial dispersion of acoustic wave velocities measured in this study agrees well with the velocities derived on the basis of natural portlandite elastic constants measured by Speziale et al. [4] (cf. Fig. 7, red line). Thus, it can be stated that at least for this kind of measurements adequate specimens comparable to natural $\text{Ca}(\text{OH})_2$ crystals were grown in the laboratory. The stiffness constants C_{ij} show only marginal differences to the components measured for natural portlandite (Table 2). An exception is C_{14} , which is a measure for the anisotropy within the basal plane [21]. It is less than half (this study) compared to data reported by Speziale et al. [4]. It is assumed that the difference is mostly due to the different spatial distribution of the sets of directions probed in the two studies. The combination of an axial plane with a truly basal one and a better quality of the signal in the new set of measurements suggest the value of C_{14} presented in this study is more accurate than that of [4]. In any case, such differences of individual elastic constants mostly vanish when calculating the averaged elastic moduli for a hypothetical isotropic polycrystal, cf. Table 3 [66]. Significant differences in the elastic components determined in this study and by Speziale et al. [4] for natural $\text{Ca}(\text{OH})_2$ exist with respect to Brillouin data on synthetic portlandite measured by Holuj et al. [22]. Especially the component C_{13} differs $> 200\%$, but also C_{12} is reported $\sim 20\%$ higher than measured in this study (Table 2). These deviations are likely caused by the small number of crystal orientations measured by Holuj et al. [22] compared to the large number of velocities determined in this study and by Speziale et al. [4].

The kinetics of the dehydration of hydrates such as portlandite and of minerals containing water in their crystal structure depends on numerous different factors [67]. Due to that, data on dehydration kinetics, i.e. above all the temperature of dehydration/decomposition, can vary quite significantly often resulting in a wide temperature range (e.g.

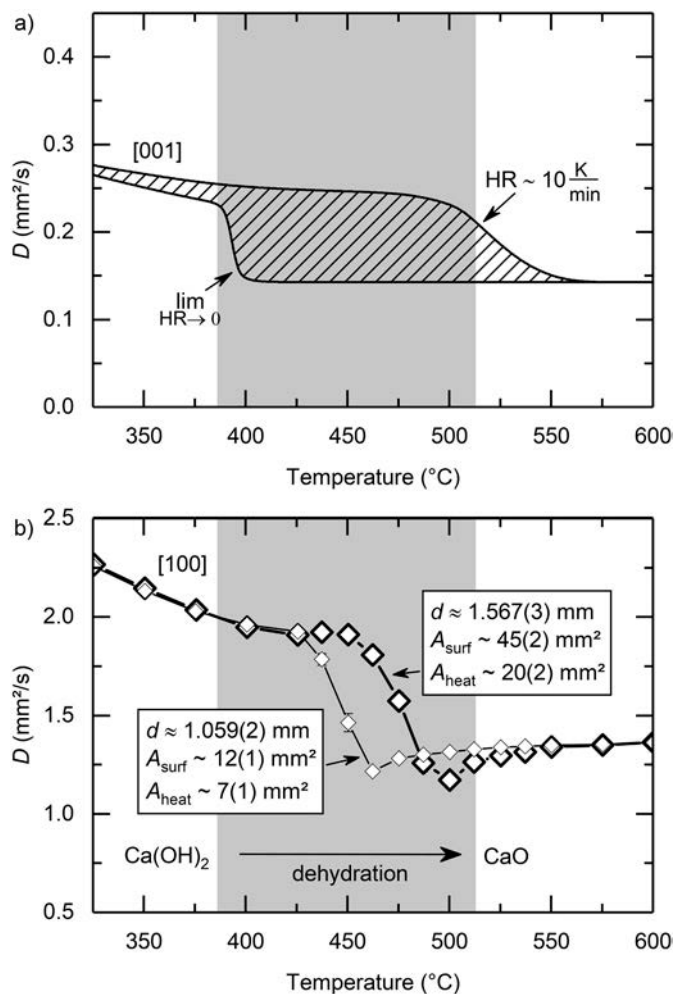


Fig. 13. Influence of experimental conditions on the dehydration and thermal diffusivity D of portlandite. a) Boundary conditions for heating rates (HR) $\lim_{HR \rightarrow 0}$ and $HR \sim 10 \text{ K/min}$, shown for the basal plane orientation. b) Influence of the specimen dimensions on D (\perp c -axis, axial plane) measured by laser flash method (axial plane, $HR \sim 3 \text{ K/min}$). A_{surf} is the platelets' surface area, A_{heat} is the area heated by the laser pulse. The gray shaded area corresponds to the dehydration temperature according to TG & DSC measurements (see Sections 2.1 & 3.2, Fig. 10b).

[68–70]). To give an estimation on how strong the thermal diffusivity with dehydration of single crystal portlandite can vary due to selected experimental conditions, two major influencing factors are considered: 1) the heating rate (HR) and 2) the influence of the particle/crystal size. For the former, two specimens (basal plane) of comparable size ($d \sim 0.7 \text{ mm}$, $\sim 4.5 \text{ mm}$ cross section) were measured by the laser flash method with $\sim 3 \text{ h}$ isothermal segments per temperature step (representing $\lim_{HR \rightarrow 0}$) on the one hand and a high heating rate of $\sim 10 \text{ K/min}$ on the other hand. The resulting effect of heating rates on the measured thermal diffusivity around the dehydration of portlandite crystal platelets is shown Fig. 13a. For the influence of the particle/crystal size, two axial plane specimens markedly different in size (see Fig. 13b for details) were measured by the laser flash method (all other conditions being equal). Comparing the two heating rate boundaries shown for the example of the basal plane orientation (Fig. 13a), significant differences in the temperature dependence of the thermal diffusivity become apparent. While the release of water is completed at a temperature of around $\sim 390^\circ\text{C}$ for $\lim_{HR \rightarrow 0}$ and the thermal diffusivity decreases to $D_{[001]} = 0.15(1) \text{ mm}^2/\text{s}$, D values for high heating rates lie up to ~ 60 – 65% above at about $D_{[001]} \approx 0.24$ – $0.25(2) \text{ mm}^2/\text{s}$ ($T = 400$ – 475°C). This discrepancy may originate from a non-homogeneous

temperature distribution within the platelet subject to heating at high HR and thus reflect the thermal diffusivity of an effective lower temperature than measured by the thermocouple just next to the specimen. Due to the lacking ability of specimen temperature equilibration, high heating rates lead to a dehydration reaction extended over a wide temperature range visible at ~ 475 °C reaching up to ~ 575 °C (Fig. 13a), *i.e.* up to ~ 185 °C above the dehydration temperature approximated for $\lim_{HR \rightarrow 0}$ with the laser flash method. Another factor influencing the dehydration temperature and correspondingly the thermal diffusivities is the specimen size. Fig. 13b shows that for the smaller crystal platelet the onset of dehydration at $T = 425$ °C is ~ 25 °C below that of the bigger specimen. In general, it can be seen that the evolution of the thermal diffusivity with temperature is shifted by ~ 25 – 30 °C comparing both specimen dimensions shown in Fig. 13b. These observed differences are expected to be even stronger for greater crystal size differences and might be transferred to powdered samples as well as to components of *e.g.* hydrated cements. In Fig. 13 it is shown that the sample dimensions and experimental conditions can impact the results of thermal transport determination. Accordingly, studies on *e.g.* portlandite for thermochemical storage systems need to carefully take into account such influencing factors as they may significantly bias the results.

The thermal diffusivity data of portlandite show a temperature dependence roughly proportional to $1/T$ for both directions [001] and [100] up to ~ 400 °C as being expected for 3-phonon umklapp processes [72,73]. The trend might be described by a modified Eucken's law $D(T) = AT^{-B}$ (T in K, after Seipold [61], see also [74]) for the contribution of lattice phonons to heat transport. Fits from -100 °C to 380 °C describe well the measured thermal diffusivity data (dashed black

lines Fig. 14a & c, shown up to $T = 650$ °C for illustration, fit parameters are shown in Table 4).

For the high temperature region, approximations $\propto T^{-B}$ lead to a thermal diffusivity vanishing for $\lim_{T \rightarrow \infty}$. But, with respect to the thermal diffusivity D (and conductivity κ) provided by lattice phonons, it seems to be more appropriate that D (and κ) reaches the so-called Einstein limit with D_0 (κ_0) > 0.0 mm^2/s ($\text{Wm}^{-1}\text{K}^{-1}$) [75] as the mean free path length l cannot become arbitrarily short (*e.g.* [71,76,77]). An approximation for the temperature dependence of D (and κ) including a lower limit for high temperatures is proposed by Roufousse and Klemens [71]. Rearranged for D_0 and κ_0 , it is

$$\begin{aligned} D(T) &= T_D T^{-3/2} + D_0 \\ \kappa(T) &= T_\kappa T^{-3/2} + \kappa_0 \end{aligned} \quad (9)$$

with T_D and T_κ fitting constants and T in Kelvin. In a first approximation, the Einstein limit of thermal diffusivity D_0 and thermal conductivity κ_0 can be predefined using the directional minimum bond length (l_0) inside the unit cell as the lower limit of mean free path length l . In *c*-axis direction [001], $l_0 \approx 0.96$ Å for O–H bond, whereas in [100] direction $l_0 \approx 2.37$ Å for the Ca–O bond of the octahedral layer (after [51]). Using (*e.g.* [73,77,78])

$$\begin{aligned} D_0 &= \frac{1}{3} \nu l_0 \\ \kappa_0 &= \frac{1}{3} \rho c_p \nu l_0 \end{aligned} \quad (10)$$

with ν phononic velocity approximated by $\nu_{mean} = \sqrt{(\nu_p^2 + \nu_{s1}^2 + \nu_{s2}^2)}/3$, the lower limit in thermal diffusivity D_0 is $0.09(1)$ mm^2/s and $0.37(1)$ mm^2/s in [001] and [100] direction, respectively. For the thermal

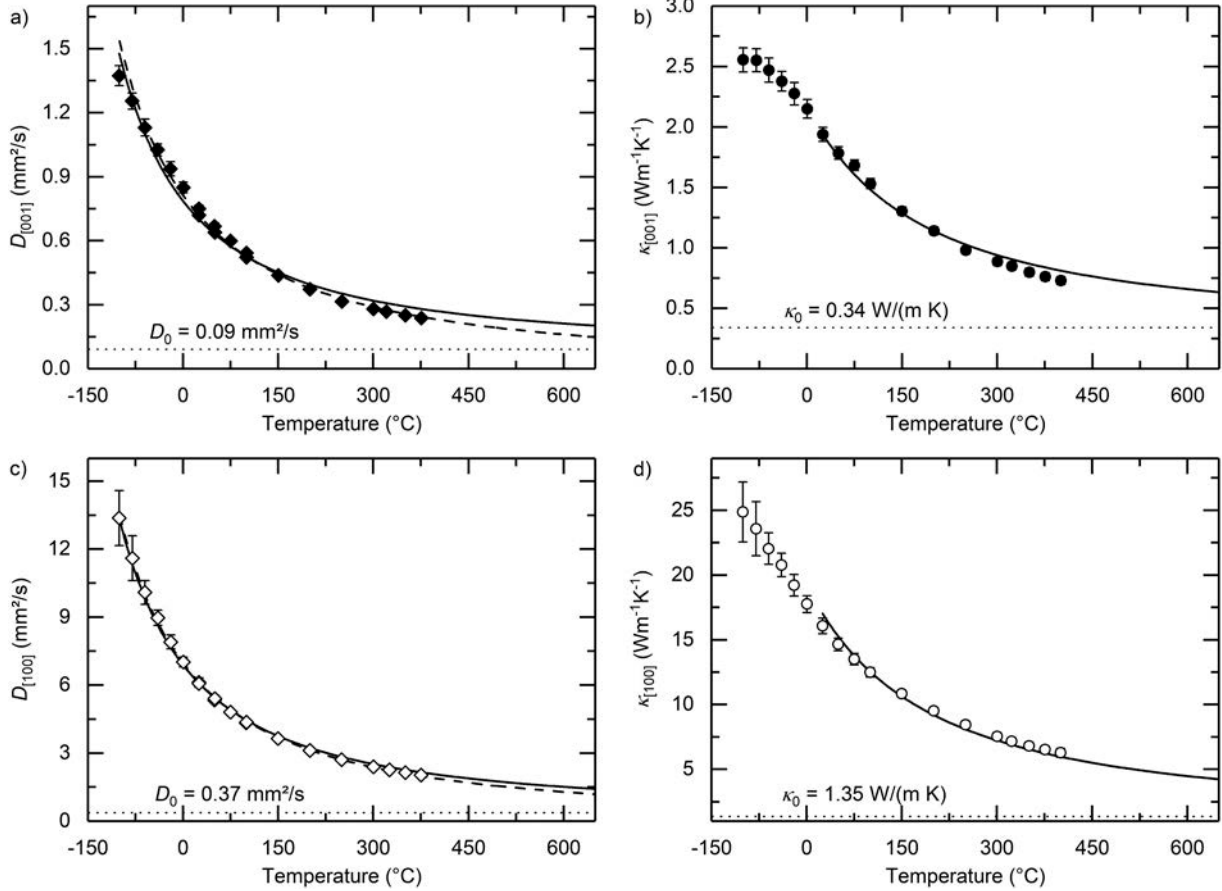


Fig. 14. Data approximation for the temperature dependence of portlandite thermal diffusivity (left: a, c) and thermal conductivity (right: b, d) in [001] (top) and [100] (bottom) direction. Dashed lines (a, c) represent fits according to $D(T) = AT^{-B}$ (after [61]). Solid lines represent data fits including predefined high temperature limits D_0 and κ_0 (dotted lines, Eq. (10)) after Roufousse and Klemens [71] (Eq. (9)). Fit parameters are shown in Table 4. For details, see text.

Table 4

Parameters for data approximations shown in Fig. 14 for the thermal diffusivity D and thermal conductivity κ , respectively. T in K, R^2 is ≥ 0.98 for all fits.

	$D(T) = AT^{-B}$ (mm ² /s)	$D(T) = T_D T^{-3/2} + D_0$ (mm ² /s)	$\kappa(T) = T_c T^{-3/2} + \kappa_0$ (Wm ⁻¹ K ⁻¹)
[100]	$24.0(31) \times 10^3 T^{-1.45(2)}$	$29.4(2) \times 10^3 T^{-3/2} + 0.37(1)$	$80.7(11) \times 10^3 T^{-3/2} + 1.35(6)$
[001]	$2.03(69) \times 10^3 T^{-1.39(6)}$	$3.14(6) \times 10^3 T^{-3/2} + 0.09(1)$	$8.2(2) \times 10^3 T^{-3/2} + 0.34(2)$

conductivity, $\kappa_0 = 0.34(2)$ Wm⁻¹K⁻¹ in [001] direction and 1.35(6) Wm⁻¹K⁻¹ in [100] direction (high T approximation $\rho c_p = 3.6 \times 10^6$ Wm⁻³K⁻¹). The resultant approximations for the temperature dependence of the thermal diffusivity (and thermal conductivity, for $T > 298$ K) only depend on a single parameter T_D (T_c) and are shown in Fig. 14, the corresponding fit parameters are given in Table 4. Data fits for thermal diffusivity (Fig. 14, left) and thermal conductivity (right) are of comparable quality for respective directions. It shows that for the axial plane orientation the fits are of slightly better quality. Compared to the previously mentioned two-parameter model $D(T) = AT^{-B}$ (after [61], dashed black lines Fig. 14a & c), the one-parameter (with fixed D_0 , κ_0) approximations using Eq. (9) are of only marginally lower quality. Hence, using a minimum in crystal bond length as the lower limit for the mean free path length l in combination with the model proposed by Roufosse and Klemens [71] fits well the observed data. This suggests that the main structural element controlling heat diffusion in single crystal portlandite in [001] direction at least at high temperatures is the hydroxyl group and thus the hydrated interlayer (series circuit of low conducting hydroxyl group interlayers and higher conducting [CaO₆] octahedral layers). In contrast, heat diffusion perpendicular to the c -axis can be well described if the [CaO₆] octahedral layers dominate the heat transport in this direction, comparable to a parallel circuit.

The thermal conductivity κ at low temperatures cannot be well described by a model $\propto 1/T$ (cf. Fig. 14b & d). This is likely due to the strong temperature dependence of the heat capacity c_p as it evolves towards a $\propto T^3$ behavior in the lower temperature region (*i.e.* well below the Debye temperature $\theta_D \sim 100$ °C [79]) as a consequence of phonon modes “freezing out” (*e.g.* [80]).

Commonly, thermal diffusivity measurements by the laser flash method on single crystalline matter are presumed to be independent of the probed specimen thickness d . This holds true as long as optically thick conditions exist. According to Hofmeister [81], specimen thicknesses ordinarily measured using laser flash method can be optically thick for fundamental IR modes but optically thin for overtone modes. Thus, depending on the particular material a thickness dependence of the thermal diffusivity can exist (*‘intrinsic length dependence’*). To approximate this effect, Hofmeister [81] suggests:

$$D(d) = D_\infty [1 - \exp(-\gamma d)] \quad (11)$$

with a fitting constant γ and the thermal diffusivity D_∞ for a material of infinite thickness. To assess the single crystal portlandite thermal diffusivity data collected in this study, basal plane specimens with varying thicknesses from $d \approx 0.14$ mm to $d \approx 1.25$ mm were measured at $T = -100$ °C, -40 °C, 25 °C and 100 °C. The results show a pronounced dependence on the thickness d of the measured thermal diffusivity at all temperatures considered (Fig. 15). To approximate this trend, Eq. (11) is adapted by adding the Einstein limit for minimum thermal diffusivity D_0 ($= 0.09(1)$ mm²/s in [001], see above). This is for the case that $\lim_{d \rightarrow 0}$, taking into account that the mean free path length l cannot fall below the minimum lattice bond distance (≈ 0.96 Å, O–H bond in [001] direction, see above):

$$D(d) = D_\infty [1 - \exp(-\gamma d)] + D_0 \quad (12)$$

(note: the thermal diffusivity limit for an infinite thick specimen is in this case $D_\infty + D_0$). Using Eq. (12) with γ being equal for all temperatures, the observed trend is well approximated (black lines, Fig. 15). But, transparent specimens need to be coated for laser pulse

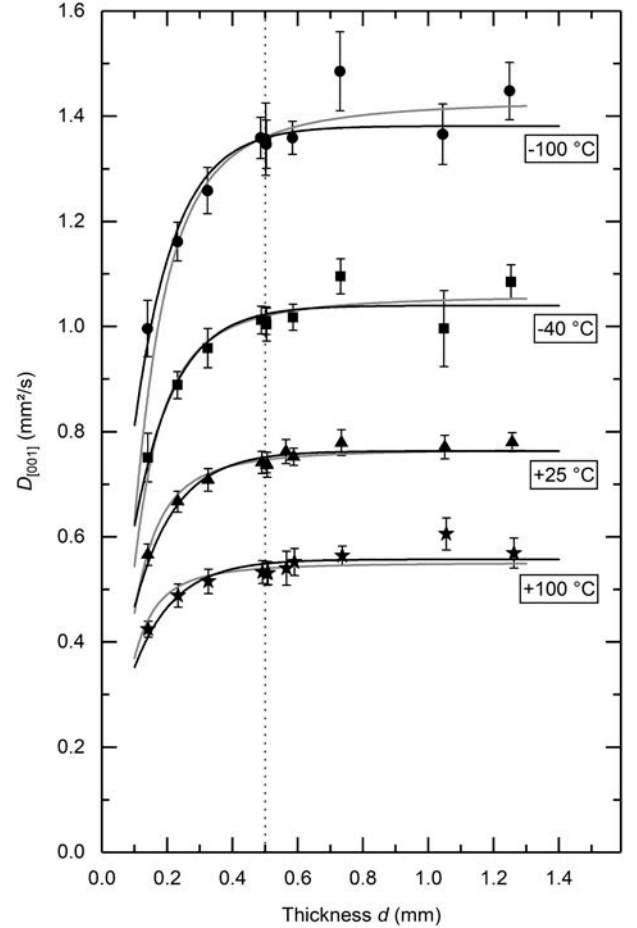


Fig. 15. Dependence of the thermal diffusivity D on the specimen thickness d for single crystal portlandite in basal plane orientation. Black lines: least-square fits using a model proposed by Hofmeister [81] adapted by adding $D_0 = 0.09(1)$ mm²/s (cf. Eq. (12)). Comparable results are obtained using an approach that takes into account the influence of the applied graphite coating in signal-time curves of measured thermal diffusivity of portlandite (gray, Eq. (13)). The dotted line corresponds to the minimum specimen thickness used for the results presented in Section 3.2.

absorption in LFA measurements (see Section 2.3) and it is known that applied coatings can affect the thermal diffusivity measurements (*e.g.* [49,82,83]). Therefore, it seems reasonable to evaluate whether the observed $D(d)$ dependence (Fig. 15) could also be explained by a coating related influence for different specimen thicknesses. Even though including coating effects in thermal diffusivity evaluation routines is non-trivial [84,85], in a first approximation $D(d)$ is fitted using

$$D(d) = 0.1388 \frac{d^2}{t_{1/2} + \Delta t} \quad (13)$$

where $t_{1/2} = 0.1388 d^2 / D_\infty$ and Δt represents the additional time needed for heat to travel through the applied coating. The resultant fits (Fig. 15, gray lines) represent well the observed trend of a decreasing apparent thermal diffusivity with decreasing specimen thickness and

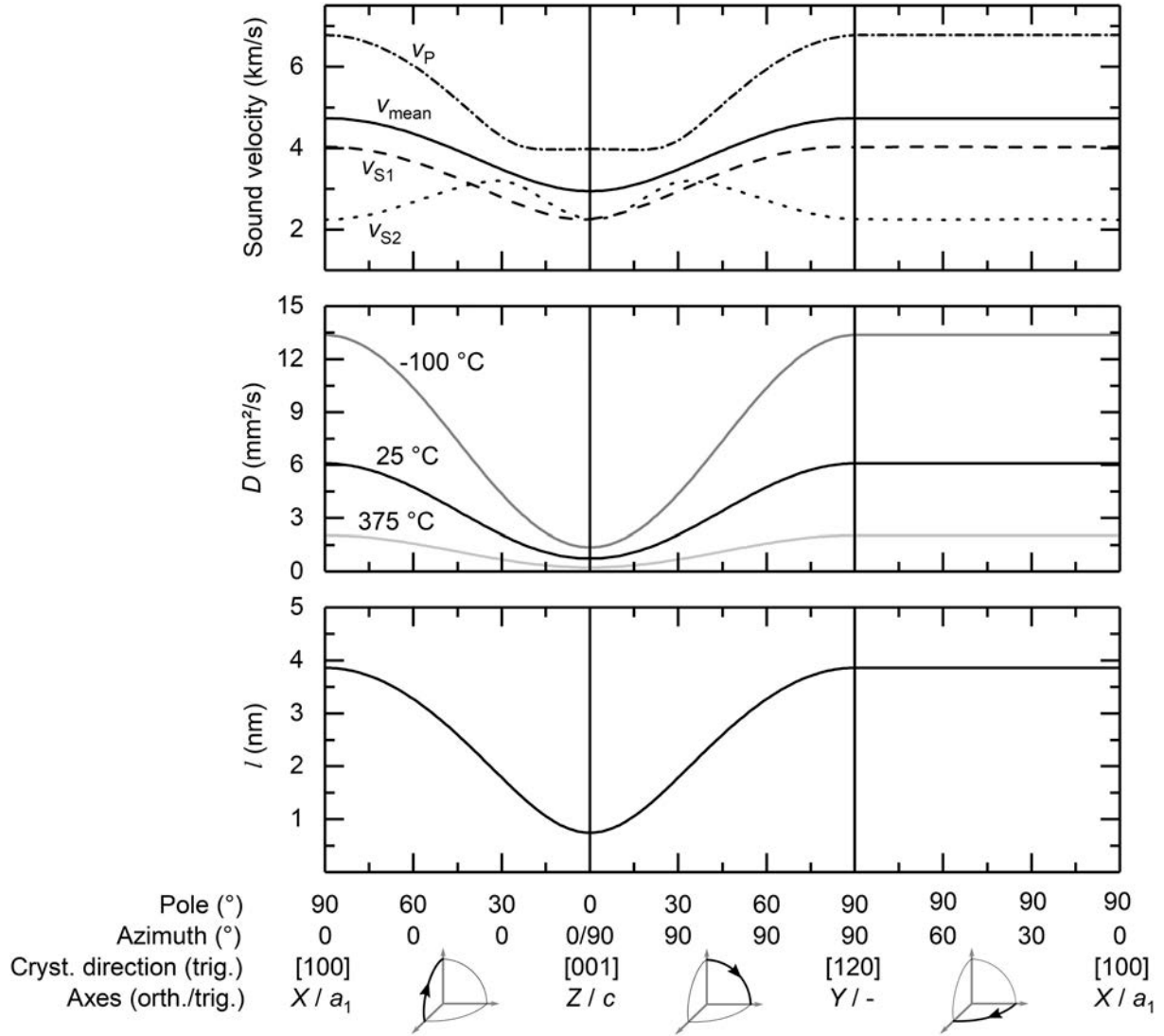


Fig. 16. Spatial distribution of elastic (acoustic sound velocities at ambient conditions) and thermal transport properties (thermal diffusivity D) of portlandite for selected orientations. Mean free path length derived as $l=3D/v$ (cf. Eq. (10), v approximated by $v_{mean} = \sqrt{(v_p^2 + v_{s1}^2 + v_{s2}^2)}/3$ at ambient conditions). The thermal diffusivity is shown for $T = -100$ °C, 25 °C and 375 °C illustrating the temperature dependence of thermoelastic properties.

are of comparable quality to approximations using Eq. (12). For thicknesses $d \geq 0.5$ mm thermal the diffusivities $D_{[001]}$ approach a constant value. The increase of D for $d \geq 0.5$ mm is small and within the experimental uncertainties independent of the chosen approximation. Our specimens for collecting thermal transport data (*i.e.* tensor components D_{ij} , derived κ_{ij} and its temperature dependencies, see Section 3.2) have a minimum thickness of $d = 0.5$ mm for the basal plane. Thus, it can be stated that at least for $D_{[001]}$ the specimen thicknesses have no significant influence on the measured thermal diffusivities and derived conductivities. In direction $\perp c$ -axis, thermal diffusivities are considerably higher (*cf.* Figs. 10 & 11) associated with a reduced $t_{1/2}$. The applied coating will thus have a stronger influence on the thermal diffusivity and D_∞ for an infinite thick sample would be reached for higher thicknesses d . On the other hand, measured axial plane specimens are thicker ($d = 1.0$ to 1.7 mm) than basal plane platelets, counteracting the thickness influence on thermal diffusivity. In conclusion, for the thermal transport properties in the axial plane direction [100] reported here (Section 3.2, *e.g.* Fig. 10, Appendices A & B) it cannot be excluded that a (significant) thickness dependence inheres the data. Thus, intrinsic heat transport and temperature equilibration $\perp c$ -axis as well as the derived anisotropies $D_{[100]}/D_{[001]}$ and $\kappa_{[100]}/\kappa_{[001]}$

might be even higher than reported. In other words, the presented values are rather lower bounds for the heat transport properties as well as for the anisotropy.

In Fig. 16 acoustic sound velocities are shown together with the thermal diffusivity D and derived mean free path length $l (= 3D/v, cf. Eq. (10))$ over three distinct crystallographic directions. The elastic properties such as v_{mean} (and also Young's modulus, see Fig. 9) and the thermal transport properties run parallel showing a pronounced anisotropy. With respect to the thermal diffusivity D at $T = -100$ °C, 25 °C and 375 °C (black and gray, Fig. 16), the strong temperature dependence of thermal transport properties is presented as an example. The maximum in thermal transport properties coincides with the direction $\perp c$ -axis reflecting the important role of the $[\text{CaO}_6]$ octahedral layers in contrast to the 3-fold axis [001] direction with strong bonds of octahedral layers in alternation with weak interlayer bonding. The thermal transport properties thus greatly correlate with the crystal structure of portlandite (*cf.* Fig. 1).

5. Conclusion

Thermoelastic properties of synthetic portlandite $\text{Ca}(\text{OH})_2$ single

crystals have been studied in detail.

Both the elastic and thermal transport data show a pronounced anisotropy with faster acoustic wave velocities, larger Young's modulus and higher thermal diffusivity and thermal conductivity in the direction perpendicular to the 3-fold axis. The spatial distribution of these properties correlates with the layered structure of $\text{Ca}(\text{OH})_2$.

A series of measurements with different specimen thicknesses reveals a distinct thickness dependency of the thermal diffusivity, which could be related to the influence of the applied specimen coating. In a comparable manner, the dehydration of $\text{Ca}(\text{OH})_2$ to CaO is strongly dependent on the experimental conditions and particularly affected by the crystal/specimen size and the chosen heating rate. This has significant impact on the measured thermal diffusivities within the temperature range of portlandite dehydration and thus should be taken into account for prospective investigations.

The strong temperature dependence and high anisotropy of the thermoelastic properties of single crystal portlandite measured in this study holds potential for further developments of innovative applications. As an example in civil engineering, in case of a controllable growth direction of portlandite (and also ettringite, see [86]) crystals during the hydration of cement pastes, intended anisotropic components for constructions are certainly conceivable. With respect to future use of portlandite in flue gas cleaning combustion technology, the detailed knowledge of thermal conductivity and thermal diffusivity provides a basis for new system designs and for refining modeling approaches related to technical processes. In particular the relationship between temperature-dependent thermal transport properties and the crystallographic orientations could contribute to innovations concerning the process design. Lastly, numerical studies on portlandite for thermochemical storage systems often assume constant and orientation independent (*i.e.* isotropic) thermal transport properties. But, measurements shown here reveal not only a high temperature variation but also a strong orientation dependent thermal transport properties for portlandite. Thus, assumptions on thermal transport properties being isotropic and constant over a wide temperature range seem to be inappropriate. The data collected in this study therefore contribute to better and more meaningful numerical studies of technical processes

Appendix A. Measured thermal diffusivities

Table A.5

Thermal diffusivities D of synthetic single crystal portlandite in [100] (axial plane) and [001] (basal plane) direction measured by laser flash method. The data are the averages of five basal and six axial specimens with at least 3 independent measurements per temperature step and specimen. Data from $-100\text{ }^\circ\text{C}$ to $100\text{ }^\circ\text{C}$ were measured by low T HgCdTe (MCT) IR detector, from $25\text{ }^\circ\text{C}$ to $700\text{ }^\circ\text{C}$ by high T setup with InSb IR detector.

T ($^\circ\text{C}$)	$D_{[100]}$ ($=D_{11} = D_{22}$) (mm^2/s)	T ($^\circ\text{C}$)	$D_{[001]}$ ($=D_{33}$) (mm^2/s)
-100.6	13.4(12)	-100.5	1.37(5)
-80.0	11.6(10)	-80.2	1.25(4)
-59.8	10.1(5)	-60.0	1.13(4)
-39.6	9.0(3)	-40.0	1.03(3)
-19.6	7.9(3)	-19.9	0.94(3)
0.3	7.0(2)	0.2	0.85(3)
25.0	6.1(2) ^a	25.1	0.75(2) ^a
25.1	6.1(2)	25.1	0.72(2)
50.0	5.4(2) ^a	49.7	0.67(1) ^a
49.0	5.3(1)	50.1	0.64(1)
75.0	4.81(12) ^a	75.0	0.60(1) ^a
99.8	4.34(9)	100.0	0.52(1)
100.1	4.36(11) ^a	100.1	0.54(1) ^a
149.9	3.64(7)	150.2	0.44(1)
199.9	3.11(6)	200.3	0.37(1)
250.1	2.71(7)	250.4	0.32(1)
300.4	2.39(8)	300.4	0.28(1)
325.4	2.26(8)	320.5	0.27(1)
350.5	2.14(8)	350.5	0.25(1)

(continued on next page)

based on portlandite as reactive medium.

CRediT authorship contribution statement

S. Breuer:Conceptualization, Methodology, Software, Formal analysis, Investigation, Resources, Data curation, Writing - original draft, Writing - review & editing, Visualization, Project administration.**M. Schwotzer:**Conceptualization, Investigation, Data curation, Writing - review & editing.**S. Speziale:**Validation, Investigation, Resources, Data curation, Writing - review & editing.**F.R. Schilling:**Conceptualization, Supervision, Methodology, Formal analysis, Investigation, Resources, Writing - review & editing.

Declaration of competing interest

The authors declare that they have no known competing financial interests or personal relationships that could have appeared to influence the work reported in this paper.

Acknowledgment

This study was made possible by a Dr. M. Herrenknecht foundation. The authors want to thank R.M. Danisi for developing a SC-XRD routine to measure angular misorientations of the portlandite platelets and A. Wunsch and D. Seiler for their initial experiments of portlandite crystal growth. Thanks to B. Oetzel, E. Eiche and M. Denker for performing ICP-MS, XRD, CSA and IC measurements. The authors furthermore acknowledge F. Krause for help performing TG and DSC measurements and L. Pennacchioni for help performing Brillouin scattering measurements. We moreover want to thank the anonymous reviewers for their effort and helpful comments on the manuscript.

Funding

This research did not receive any specific grant from funding agencies in the public, commercial, or not-for-profit sectors.

Table A.5 (continued)

T (°C)	$D_{[100]} (=D_{11} = D_{22})$ (mm ² /s)	T (°C)	$D_{[001]} (=D_{33})$ (mm ² /s)
375.5	2.04(8)	375.6	0.24(1)
400.4	1.96(10)	400.6	0.23(1)
425.4	1.86(11)	425.5	0.22(1)
437.3	1.65(15)	437.3	0.22(1)
450.3	1.37(13)	450.3	0.21(1)
462.3	1.24(8)	462.1	0.21(1)
475.3	1.25(7)	475.3	0.20(1)
487.3	1.30(7)	487.2	0.18(1)
500.3	1.30(6)	500.3	0.15(1)
512.2	1.31(5)	512.2	0.14(1)
525.3	1.31(5)	525.2	0.14(1)
537.2	1.32(4)	537.2	0.15(1)
550.2	1.32(5)	550.2	0.14(1)
575.4	1.32(6)	575.3	0.15(1)
600.4	1.32(8)	600.3	0.15(1)
650.4	1.34(11)	650.3	0.15(1)
700.3	1.39(9)	700.2	0.17(1)

^a Thermal diffusivity values measured by HgCdTe (MCT) IR detector in the overlapping T region between 25 °C to 100 °C

Appendix B. Derived thermal conductivities

Table B.6

Thermal conductivity tensor κ_{ij} for single crystal portlandite derived using Eq. (5) along [100] ($=\kappa_{11} = \kappa_{22}$) and in perpendicular c -axis direction [001] ($=\kappa_{33}$).

T (°C)	κ_{11} (Wm ⁻¹ K ⁻¹)	κ_{33} (Wm ⁻¹ K ⁻¹)	ρ (g/cm ³)	c_p (Jkg ⁻¹ K ⁻¹)
-100.6	24.9(23)	2.55(10)	2.261	823
-80.1	23.6(21)	2.55(9)	2.257	901
-59.9	22.0(12)	2.47(10)	2.254	969
-39.8	20.8(9)	2.38(8)	2.250	1030
-19.8	19.2(8)	2.28(9)	2.247	1081
0.2	17.8(7)	2.15(8)	2.243	1128
25.1	16.1(6)	1.94(6)	2.239	1178
49.9	14.6(5)	1.78(5)	2.235	1221
75.0	13.5(4)	1.68(4)	2.231	1258
100.0	12.5(4)	1.53(4)	2.226	1290
150.0	10.8(3)	1.30(3)	2.218	1343
200.1	9.5(3)	1.14(3)	2.210	1382
250.3	8.4(3)	0.98(3)	2.201	1413
300.4	7.5(3)	0.89(3)	2.193	1438
322.9	7.2(3)	0.85(3)	2.189	1447
350.5	6.8(3)	0.80(3)	2.185	1459
375.6	6.5(3)	0.76(3)	2.181	1467
400.5	6.3(3)	0.73(3)	2.176	1476

The temperature-dependent densities ρ are approximated on the basis of the density measured by XRD at 20 °C ($\rho = 2.240(2)$ g/cm³, see Section 2.1) using linear thermal expansion coefficients α_L for portlandite given by Xu et al. [51] extrapolated for the given temperature range from -100 °C to 400 °C: α_1 -axis $\alpha_{L,a} = 1.1759 \times 10^{-5}$ 1/K and c -axis $\alpha_{L,c} = 5.2548 \times 10^{-5}$ 1/K.

Listed isobaric heat capacities c_p for portlandite are taken from Chase [63] (based on Kobayashi 1950 (cited by [63]) and Hatton et al. [64], 1 σ assumed as 2%) and $M_{\text{Ca(OH)}_2} = 74.093$ g/mol was used for calculations.

References

- [1] C. Meade, R. Jeanloz, Static compression of Ca(OH)₂ at room temperature: observations of amorphization and equation of state measurements to 10.7 GPa, *Geophys. Res. Lett.* 17 (1990) 1157–1160, <https://doi.org/10.1029/GL017i008p01157>.
- [2] J.D. Birchall, A.J. Howard, J.A. Bailey, On the hydration of Portland cement, *Proceedings of the Royal Society of London A-Mathematical and Physical Sciences* 360 (1978) 445–453, <https://doi.org/10.1098/rspa.1978.0078>.
- [3] P.-C. Aitcin, Portland cement, in: P.-C. Aitcin, R.J. Flatt (Eds.), *Science and Technology of Concrete Admixtures*, Woodhead Publishing, 2016, pp. 27–51, <https://doi.org/10.1016/B978-0-08-100693-1.00003-5>.
- [4] S. Speziale, H.J. Reichmann, F.R. Schilling, H.R. Wenk, P.J.M. Monteiro, Determination of the elastic constants of portlandite by Brillouin spectroscopy, *Cem. Concr. Res.* 38 (2008) 1148–1153, <https://doi.org/10.1016/j.cemconres.2008.05.006>.
- [5] J.M. Bigham, D.A. Kost, R.C. Stehouwer, J.H. Beeghly, R. Fowler, S.J. Traina, W.E. Wolfe, W.A. Dick, Mineralogical and engineering characteristics of dry flue gas desulfurization products, *Fuel* 84 (2005) 1839–1848, <https://doi.org/10.1016/j.fuel.2005.03.018>.
- [6] C.-F. Liu, S.-M. Shih, Effects of flue gas components on the reaction of Ca(OH)₂ with SO₂, *Ind. Eng. Chem. Res.* 45 (2006) 8765–8769, <https://doi.org/10.1021/ie0605534>.
- [7] H. Wang, D. Chen, Z. Li, D. Zhang, N. Cai, J. Yang, G. Wei, SO₃ removal from flue gas with Ca(OH)₂ in entrained flow reactors, *Energy Fuel* 32 (2018) 5364–5373, [doi:https://doi.org/10.1021/acs.energyfuels.8b00274](https://doi.org/10.1021/acs.energyfuels.8b00274), publisher: American Chemical Society.
- [8] S.-M. Shih, C.-S. Ho, Y.-S. Song, J.-P. Lin, Kinetics of the reaction of Ca(OH)₂ with CO₂ at low temperature, *Ind. Eng. Chem. Res.* 38 (1999) 1316–1322, [doi:https://doi.org/10.1021/ie9805534](https://doi.org/10.1021/ie9805534).

- doi.org/10.1021/ie980508z.
- [9] M.J. Renedo, C. Pesquera, F. Gonzalez, J. Fernandez, Use of TG-DSC-MS and gas analyzer data to investigate the reaction of CO₂ and SO₂ with Ca(OH)₂ at low temperature, *Chem. Eng. Trans.* 35 (2013) 739–744, <https://doi.org/10.3303/CET1335123>.
- [10] I. Fernández, A. Garea, A. Irabien, SO₂ reaction with Ca(OH)₂ at medium temperatures (300–425°C): kinetic behaviour, *Chem. Eng. Sci.* 53 (1998) 1869–1881, [https://doi.org/10.1016/S0009-2509\(98\)00029-3](https://doi.org/10.1016/S0009-2509(98)00029-3).
- [11] G.G. Li, T.C. Keener, A.W. Stein, S.J. Khang, CO₂ reaction with Ca(OH)₂ during SO₂ removal with convective pass sorbent injection and high temperature filtration, *Environmental Engineering and Policy* 2 (1999) 47–56, <https://doi.org/10.1007/BF03500906>.
- [12] M. Schmidt, Experimental Investigation of Ca(OH)₂ As Thermochemical Energy Storage at Process Relevant Boundary Conditions, Dissertation University of Stuttgart, Stuttgart, Germany, 2017.
- [13] Q.A. Ranjha, N. Vahedi, A. Oztekin, Numerical study of thermochemical storage using Ca(OH)₂/CaO: high temperature applications, Volume 6B: Energy, American Society of Mechanical Engineers, Phoenix, Arizona, USA, 2016, <https://doi.org/10.1115/IMECE2016-65909>.
- [14] F. Holuj, C.T. Kwan, Polytropy and the ESR of Fe³⁺ in Ca(OH)₂, *J. Magn. Reson.* 18 (1975) 123–128, [https://doi.org/10.1016/0022-2364\(75\)90230-9](https://doi.org/10.1016/0022-2364(75)90230-9).
- [15] M.B. Kruger, Q. Williams, R. Jeanloz, Vibrational spectra of Mg(OH)₂ and Ca(OH)₂ under pressure, *J. Chem. Phys.* 91 (1989) 5910–5915, <https://doi.org/10.1063/1.457460>.
- [16] L. Desgranges, G. Calvarin, G. Chevrier, Interlayer interactions in M(OH)₂: a neutron diffraction study of Mg(OH)₂, *Acta Crystallographica Section B Structural Science* 52 (1996) 82–86, <https://doi.org/10.1107/S0108768195008275>.
- [17] T. Nagai, T. Ito, T. Hattori, T. Yamanaka, Compression mechanism and amorphization of portlandite, Ca(OH)₂: structural refinement under pressure, *Phys. Chem. Miner.* 27 (2000) 462–466, <https://doi.org/10.1007/s002690000084>.
- [18] L. Desgranges, D. Grebille, G. Calvarin, G. Chevrier, N. Floquet, J.-C. Niepce, Hydrogen thermal motion in calcium hydroxide: Ca(OH)₂, *Acta Crystallographica Section B Structural Science* 49 (1993) 812–817, <https://doi.org/10.1107/S0108768193003556>.
- [19] K. Momma, F. Izumi, VESTA 3 for three-dimensional visualization of crystal, volumetric and morphology data, *J. Appl. Crystallogr.* 44 (2011) 1272–1276, <https://doi.org/10.1107/S0021889811038970>.
- [20] J.L. Laugesen, Density functional calculations of elastic properties of portlandite, Ca(OH)₂, *Cem. Concr. Res.* 35 (2005) 199–202, <https://doi.org/10.1016/j.cemconres.2004.07.036>.
- [21] G. Ulian, G. Valdrè, Equation of state and second-order elastic constants of portlandite Ca(OH)₂ and brucite Mg(OH)₂, *Phys. Chem. Miner.* 46 (2019) 101–117, <https://doi.org/10.1007/s00269-018-0989-3>.
- [22] F. Holuj, M. Drozdowski, M. Czajkowski, Brillouin spectrum of Ca(OH)₂, *Solid State Commun.* 56 (1985) 1019–1021, [https://doi.org/10.1016/0038-1098\(85\)90862-2](https://doi.org/10.1016/0038-1098(85)90862-2).
- [23] J.R. Johnston, The utilization of diffusion processes in the preparation of pure substances, *J. Am. Chem. Soc.* 36 (1914) 16–19, <https://doi.org/10.1021/ja02178a003>.
- [24] F.W. Ashton, R. Wilson, The preparation and optical properties of calcium hydroxide crystals, *Am. J. Sci.* 13 (5) (1927) 209–218, <https://doi.org/10.2475/ajs.s5-13.75.209Series>.
- [25] J.R. Johnston, F.P. Glasser, Carbonation of portlandite single crystals and portlandite in cement paste, 9th International Congress on the Chemistry of Cement, vol. 5, National Council for Cement and Building Materials, New Delhi, 1992, pp. 370–376.
- [26] A. Maciel-Camacho, H.R. Hernández, A.W.D. Hills, R.D. Morales, Hydration kinetics of lime, *ISIJ Int.* 37 (1997) 468–476, <https://doi.org/10.2355/isijinternational.37.468>.
- [27] A. Pavese, M. Catti, G. Ferraris, S. Hull, P-V equation of state of portlandite, Ca(OH)₂, from powder neutron diffraction data, *Phys. Chem. Miner.* 24 (1997) 85–89, <https://doi.org/10.1007/s002690050020>.
- [28] L. Brillouin, Diffusion de la Lumière et des Rayons X par un Corps Transparent Homogène-Influence de l'Agitation Thermique, *Ann. Phys.* 9 (1922) 88–122, <https://doi.org/10.1051/anphys/192209170088>.
- [29] L.I. Mandelstam, Light scattering by inhomogeneous media, *Zh. Radio-Fiziko-Khimicheskogo Obshchestva* 58 (1926) 381.
- [30] E. Gross, Über Änderung der Wellenlänge bei Lichtzerstreuung in Kristallen, *Z. Phys.* 63 (1930) 685–687, <https://doi.org/10.1007/BF01340308>.
- [31] R. Vacher, L. Boyer, Brillouin scattering: a tool for the measurement of elastic and photoelastic constants, *Phys. Rev. B* 6 (1972) 639–673, <https://doi.org/10.1103/PhysRevB.6.639>.
- [32] S. Speziale, H. Marquardt, T.S. Duffy, Brillouin scattering and its application in geosciences, *Rev. Mineral. Geochem.* 78 (2014) 543–603, <https://doi.org/10.2138/rmg.2014.78.14>.
- [33] C.H. Whitfield, E.M. Brody, W.A. Bassett, Elastic moduli of NaCl by Brillouin scattering at high pressure in a diamond anvil cell, *Rev. Sci. Instrum.* 47 (1976) 942–947, <https://doi.org/10.1063/1.1134778>.
- [34] J.R. Sandercock, Trends in Brillouin scattering: studies of opaque materials, supported films, and central modes, in: M. Cardona, G. Güntherodt (Eds.), *Light Scattering in Solids III: Recent Results, Topics in Applied Physics*, Springer, Berlin, Heidelberg, 1982, pp. 173–206.
- [35] S. Speziale, T.S. Duffy, Single-crystal elastic constants of fluorite (CaF₂) to 9.3 GPa, *Phys. Chem. Miner.* 29 (2002) 465–472, <https://doi.org/10.1007/s00269-002-0250-x>.
- [36] P.H. Gammon, H. Kiefte, M.J. Clouter, Elastic constants of ice samples by Brillouin spectroscopy, *J. Phys. Chem.* 87 (1983) 4025–4029, <https://doi.org/10.1021/j100244a004>.
- [37] H.Z. Cummins, P.E. Schoen, Linear scattering from thermal fluctuations, in: F.T. Arecchi, E.O. Schultz-Dubois (Eds.), *Laser Handbook*, vol. 2, North-Holland Publishing, Amsterdam, 1972, pp. 1029–1076.
- [38] A.G. Every, General closed-form expressions for acoustic waves in elastically anisotropic solids, *Phys. Rev. B* 22 (1980) 1746–1760, <https://doi.org/10.1103/PhysRevB.22.1746>.
- [39] J.F. Nye, *Physical Properties of Crystals: Their Representation by Tensors and Matrices*, Clarendon Press; Oxford University Press, Oxford, New York, (1985).
- [40] K. Levenberg, A method for the solution of certain non-linear problems in least squares, *Q. Appl. Math.* 2 (1944) 164–168, <https://doi.org/10.1090/qam/10666>.
- [41] D.W. Marquardt, An algorithm for least-squares estimation of nonlinear parameters, *J. Soc. Ind. Appl. Math.* 11 (1963) 431–441, <https://doi.org/10.1137/0111030>.
- [42] CRC Handbook of Chemistry and Physics, Taylor & Francis Ltd, in: J.R. Rumble, D.R. Lide, T.J. Bruno (Eds.), 99th edn, 2018.
- [43] C.-C. Chen, C.-C. Lin, L.-G. Liu, S.V. Sinogeikin, J.D. Bass, Elasticity of single-crystal calcite and rhodochrosite by Brillouin spectroscopy, *Am. Mineral.* 86 (2001) 1525–1529, <https://doi.org/10.2138/am-2001-11-1222>.
- [44] W.J. Parker, R.J. Jenkins, C.P. Butler, G.L. Abbott, Flash method of determining thermal diffusivity, heat capacity, and thermal conductivity, *J. Appl. Phys.* 32 (1961) 1679–1684, <https://doi.org/10.1063/1.1728417>.
- [45] L. Vozár, W. Hohenauer, Flash method of measuring the thermal diffusivity. A review, *High Temperatures-High Pressures* 35/36 (2003) 253–264, <https://doi.org/10.1068/htrj119>.
- [46] DIN EN/IEC 60584-1, Thermocouples-Part 1, EMF Specifications and Tolerances, Norm, CENELEC European Committee for Electrotechnical Standardization, CLC/TC 65X Industrial-process Measurement, Control and Automation, (2013).
- [47] S. Breuer, F.R. Schilling, Improving thermal diffusivity measurements by including detector inherent delayed response in laser flash method, *Int. J. Thermophys.* 40 (2019) 95, <https://doi.org/10.1007/s10765-019-2562-9>.
- [48] J.M. Branlund, A.M. Hofmeister, Thermal diffusivity of quartz to 1,000°C: effects of impurities and the alpha-beta phase transition, *Phys. Chem. Miner.* 34 (2007) 581–595, <https://doi.org/10.1007/s00269-007-0173-7>.
- [49] F. Cernuschi, L. Lorenzoni, P. Bianchi, A. Figari, The effects of sample surface treatments on laser flash thermal diffusivity measurement, *Infrared Physics and Technology* 43 (2002) 133–138, [https://doi.org/10.1016/S1350-4495\(02\)00131-7](https://doi.org/10.1016/S1350-4495(02)00131-7).
- [50] W. Stryczniewicz, J. Zmywaczyk, A.J. Panas, Inverse problem solution for a laser flash studies of a thin layer coatings, *International Journal of Numerical Methods for Heat and Fluid Flow* 27 (2017) 698–710, <https://doi.org/10.1108/HFF-03-2016-0100>.
- [51] H. Xu, Y. Zhao, S.C. Vogel, L.L. Daemen, D.D. Hickmott, Anisotropic thermal expansion and hydrogen bonding behavior of portlandite: a high-temperature neutron diffraction study, *J. Solid State Chem.* 180 (2007) 1519–1525, <https://doi.org/10.1016/j.jssc.2007.03.004>.
- [52] G. Fiquet, P. Richet, G. Montagnac, High-temperature thermal expansion of lime, periclase, corundum and spinel, *Phys. Chem. Miner.* 27 (1999) 103–111, <https://doi.org/10.1007/s002690050246>.
- [53] H. S. Carslaw, J. C. Jaeger, *Conduction of Heat in Solids*, Oxford University Press, Oxford, 2nd edn, (1959).
- [54] W. Voigt, *Lehrbuch der Kristallphysik*, B.G. Teubner, Leipzig Berlin, 1928.
- [55] A. Reuss, Berechnung der Fließgrenze von Mischkristallen auf Grund der Plastizitätsbedingung für Einkristalle, *Journal of Applied Mathematics and Mechanics/Zeitschrift für Angewandte Mathematik und Mechanik* 9 (1929) 49–58, <https://doi.org/10.1002/zamm.19290090104>.
- [56] R. Hill, The elastic behaviour of a crystalline aggregate, *Proceedings of the Physical Society. Section A* 65 (1952) 349–354, <https://doi.org/10.1088/0370-1298/65/5/307>.
- [57] J.M.J. den Toonder, J.A.W. van Dommelen, F.P.T. Baaijens, The relation between single crystal elasticity and the effective elastic behaviour of polycrystalline materials: theory, measurement and computation, *Model. Simul. Mater. Sci. Eng.* 7 (1999) 909–928, <https://doi.org/10.1088/0965-0393/7/6/301>.
- [58] W. Pabst, E. Gregorová, Effective elastic properties of alumina-zirconia composite ceramics-part 2. Micromechanical modeling, *Ceramics-Silikáty* 48 (2004) 14–23.
- [59] F.R. Schilling, *Mineralphysik-Ein Mineralogischer Ansatz*, Habilitation, Freie Universität, Berlin, Berlin, 1998.
- [60] B.P. Yur'ev, N.A. Spirin, Thermophysical properties of limestone and lime on heating, *Steel in Translation* 42 (2012) 308–311, <https://doi.org/10.3103/S0967091212040195>.
- [61] U. Seipold, Temperature dependence of thermal transport properties of crystalline rocks - a general law, *Tectonophysics* 291 (1998) 161–171, [https://doi.org/10.1016/S0040-1951\(98\)00037-7](https://doi.org/10.1016/S0040-1951(98)00037-7).
- [62] W. Woodside, J.H. Messmer, Thermal conductivity of porous media. I. Unconsolidated sands, *J. Appl. Phys.* 32 (1961) 1688–1699, <https://doi.org/10.1063/1.1728419>.
- [63] M.W. Chase (Ed.), *NIST-JANAF Thermochemical Tables*, American Chemical Society and the American Institute of Physics for the National Institute of Standards and Technology, 4th edn, Woodbury, New York, 1998.
- [64] W.E. Hatton, D.L. Hildenbrand, G.C. Sinke, D.R. Stull, The chemical thermodynamic properties of calcium hydroxide, *J. Am. Chem. Soc.* 81 (1959) 5028–5030, <https://doi.org/10.1021/ja01528a004>.
- [65] A. Eucken, Über die Temperaturabhängigkeit der Wärmeleitfähigkeit Fester Nichtmetalle, *Ann. Phys.* 339 (1911) 185–221, <https://doi.org/10.1002/andp.19113390202>.
- [66] C.-S. Zha, T.S. Duffy, R.T. Downs, H.-K. Mao, R.J. Hemley, Sound velocity and elasticity of single-crystal forsterite to 16 GPa, *Journal of Geophysical Research*:

- Solid Earth 101 (1996) 17535–17545, <https://doi.org/10.1029/96JB01266>.
- [67] A. K. Galwey, Dehydration of crystalline hydrates, in: M. E. Brown, P. K. Gallagher (Eds.), *Handbook of Thermal Analysis and Calorimetry Vol. 2: Applications to Inorganic and Miscellaneous Materials*, Elsevier, 595–656, doi:[https://doi.org/10.1016/S1573-4374\(03\)80016-X](https://doi.org/10.1016/S1573-4374(03)80016-X), 2003.
- [68] W. Jozewicz, B.K. Gullett, Reaction mechanisms of dry Ca-based sorbents with gaseous HCl, *Ind. Eng. Chem. Res.* 34 (1995) 607–612, <https://doi.org/10.1021/ie00041a022>.
- [69] F. Schaube, L. Koch, A. Wörner, H. Müller-Steinhagen, A thermodynamic and kinetic study of the de- and rehydration of Ca(OH)₂ at high H₂O partial pressures for thermo-chemical heat storage, *Thermochim. Acta* 538 (2012) 9–20, <https://doi.org/10.1016/j.tca.2012.03.003>.
- [70] D. Lager, W. Hohenauer, C. Knoll, P. Weinberger, A. Werner, Methodology to determine the apparent specific heat capacity of metal hydroxides for thermochemical energy storage, *J. Therm. Anal. Calorim.* 133 (2018) 207–215, <https://doi.org/10.1007/s10973-017-6883-2>.
- [71] M. Roufosse, P.G. Klemens, Lattice thermal conductivity of minerals at high temperatures, *J. Geophys. Res.* 79 (1974) 703–705, <https://doi.org/10.1029/JB079i005p00703>.
- [72] R. Peierls, Zur Kinetischen Theorie der Wärmeleitung in Kristallen, *Ann. Phys.* 395 (8) (1929) 1055–1101, <https://doi.org/10.1002/andp.19293950803>.
- [73] C. Kittel, *Introduction to Solid State Physics*, 8th edn., Wiley, Hoboken, NJ, 2005.
- [74] A. M. Hofmeister, J. Dong, J. M. Branlund, Thermal diffusivity of electrical insulators at high temperatures: evidence for diffusion of bulk phonon-polaritons at infrared frequencies augmenting phonon heat conduction, *J. Appl. Phys.* 115 (16, 2014) 163517 1–19, doi:<https://doi.org/10.1063/1.4873295>.
- [75] D.G. Cahill, S.K. Watson, R.O. Pohl, Lower limit to the thermal conductivity of disordered crystals, *Phys. Rev. B* 46 (1992) 6131–6140, <https://doi.org/10.1103/PhysRevB.46.6131>.
- [76] D.P. Spitzer, Lattice thermal conductivity of semiconductors: a chemical bond approach, *J. Phys. Chem. Solids* 31 (1970) 19–40, [https://doi.org/10.1016/0022-3697\(70\)90284-2](https://doi.org/10.1016/0022-3697(70)90284-2).
- [77] R. B. Berman, Clarendon Press, *Thermal Conduction in Solids*, 1976.
- [78] J.M. Ziman, *Electrons and phonons: the theory of transport phenomena in solids*, Oxford Classic Texts in the Physical Sciences, Clarendon Press; Oxford University Press, Oxford: New York, 2001.
- [79] L. Desgranges, D. Grebille, G. Calvarin, K. Chhor, C. Pommier, N. Floquet, J.C. Niepce, Structural and thermodynamic evidence of a change in thermal motion of hydrogen atoms in Ca(OH)₂ at low temperature, *J. Phys. Chem. Solids* 55 (1994) 161–166, [https://doi.org/10.1016/0022-3697\(94\)90073-6](https://doi.org/10.1016/0022-3697(94)90073-6).
- [80] R. Gross, A. Marx, *Festkörperphysik*, De Gruyter, Berlin Boston, 2nd edn. (2014).
- [81] A.M. Hofmeister, *Measurements, Mechanisms, and Models of Heat Transport*, 1st edn, Elsevier, Philadelphia, PA, 2019.
- [82] K.-H. Lim, S.-K. Kim, M.-K. Chung, Improvement of the thermal diffusivity measurement of thin samples by the flash method, *Thermochim. Acta* 494 (2009) 71–79, <https://doi.org/10.1016/j.tca.2009.04.019>.
- [83] P. Schoderböck, H. Klocker, L.S. Sigl, G. Seeber, Evaluation of the thermal diffusivity of thin specimens from laser flash data, *Int. J. Thermophys.* 30 (2009) 599–607, <https://doi.org/10.1007/s10765-009-0561-y>.
- [84] J. Hartmann, O. Nilsson, J. Fricke, Thermal diffusivity measurements on two-layered and three-layered systems with the laser-flash method, *High Temperatures-High Pressures* 25 (1993) 403–410.
- [85] N. Araki, A. Makino, J. Mihara, Measurement and evaluation of the thermal diffusivity of two-layered materials, *Int. J. Thermophys.* 13 (1992) 331–349, <https://doi.org/10.1007/BF00504441>.
- [86] S. Speziale, F. Jiang, Z. Mao, P.J.M. Monteiro, H.-R. Wenk, T.S. Duffy, F.R. Schilling, Single-crystal elastic constants of natural ettringite, *Cem. Concr. Res.* 38 (2008) 885–889, <https://doi.org/10.1016/j.cemconres.2008.02.004>.